Modelling Alkaline Silicon-Air Batteries

A Finite Element Model

R. N. van Grootel

Technische Universiteit Delft

TU Delft

(This page would be intentionally left blank if the author would not wish to inform about that)

Modelling Alkaline Silicon-Air Batteries

A Finite Element Model

by

R. N. van Grootel

to obtain the degree of Master of Science
at the Delft University of Technology,

Student number:	4370724	
Project duration:	November, 2020 – December, 2021	
Thesis committee:	Dr. R.A.C.C.M. van Swaaij,	Delft University of Technology, supervisor
	Dr. M. Ghaffarian Niasar,	Delft University of Technology
	Dr. Ir. R. Santbergen,	Delft University of Technology
	Dr. M. R. Vogt,	Delft University of Technology

An electronic version of this thesis is available at http://repository.tudelft.nl/.

TU Delft

(This page would be intentionally left blank if the author would not wish to inform about that)

Acknowledgements

I would like to utilize this space to express my thanks to some people who helped me during this thesis project. First and foremost I would like to express my deepest gratitude to my supervisor, dr. René van Swaaij, for providing me with this very interesting thesis topic, for his guidance and support throughout the process, and for his dedication for providing me with the necessary feedback, even during out-of-office hours. Eventhough the thesis needed to be restructured after several months, the backup plan that was in place has proven to be a very interesting thesis topic to investigate. Without his insights and feedback I would not have come this far in this topic.
Next, I would like to express my gratitude to dr. Malte Vogt for his help with and introduction to COMSOL. Without his help this software would have been quite a hassle. His insights during our weekly meetings were very helpful.
Third, I would like thank my fellow students in the electrical storage group of the PVMD group, Siri Gani and Tim Ammerlaan for their support in the lab, and for being a sounding board during this process. They provided much needed advise and help during the struggles that are common in thesis work.
Thanks should also go to Daragh O'Connor, Martijn Tijssen, and Can Han for their help with the technical part of the experimental work. Although the results from the experimental work were disappointing, their help was very much appreciated.
I would also like to thank Jasper Prins for making time in his busy schedule to help out with my thesis project, even though he had already finished his thesis work long before I started mine.

My parents should not be forgotten. In essence, they are the sole reason I was able to work on this thesis. Quite literally. Thank you mom and dad for your support throughout my studies. I would like to dedicate this thesis to them.

I would like to use this space to thank the people surrounding me during this process. Especially I would like to thank Chantal for being there for me during all this time and keeping me afloat. A big purr goes out to my cats. Thanks also go out to my friends from SET and my bachelors who kept me company whilst writing my thesis and who provided a listening ear during the coffee breaks. A special thanks goes out to Krullevaar for helping me out with my LaTeX code and for proof reading part of this thesis. I cannot leave the pieces of garbage that are the Caldera unmentioned. They provided some welcome distraction while I was not working on my thesis.

R. N. van Grootel
Delft, December 2021

(This page would be intentionally left blank if the author would not wish to inform about that)

Abstract

Renewable energy sources such as solar and wind energy rely on climate- and weather conditions, like sun irradiation in the case of solar energy, and wind speed in the case of wind energy. These change throughout the day and with the seasons. There are periods of little wind, and during the night there is no sunlight. During periods of no sunlight and little to no wind, there is still a demand for energy. This leads to a shortage of energy. On the other hand, there are periods when the amount of available wind- and solar energy will surpass the demand for energy, leading to an energy excess. To mitigate this mismatch between energy production and energy demand the excess energy can be stored to be used during periods of shortage. Many different solutions for this have been investigated in recent years. One of the storage technologies that is currently quite dominant is battery storage. Lithium-ion batteries are used quite widely, among others in battery electric vehicles. However, the use of batteries as a storage device to overcome energy mismatch is not yet implemented on a large scale, as most battery technologies are still quite novel, making them uneconomical for this use compared to traditional hydrocarbon fired power plants. Furthermore, many battery technologies depend on scarce and expensive minerals. Recently, a battery utilizing silicon as its anode and oxygen from the air at the cathode has been proposed. This so-called silicon-air battery utilizes mainly silicon and oxygen, which are the two most common elements on earth. Furthermore, the theoretical energy density of this battery type was shown to be significantly higher than the energy density of lithium-ion batteries. Because of this, the silicon-air battery has been a growing area of research in the last years.

Battery models help to simulate batteries based on empirical data and electrochemical systems. These models are a powerful tool in the evaluation of the performance of batteries. Parameters of the battery can be altered quickly and specifically. This can provide a powerful analysis tool to determine weaknesses in a batteries. They can also help in further developing an understanding of the operating principles of the battery technology. A specific type of model is the finite element model. In this type of model the object that is modeled is divided into small pieces and for each piece a set of (partial) differential equations is evaluated. Different electrochemical, chemical, physical and mathematical models can be modelled and combined in this tool. For this thesis a finite element model of an alkaline silicon-air battery is developed in COMSOL. The model is based on an earlier model that was developed in 2020.

Besides the discharge mechanism, alkaline silicon-air batteries are subject to two side reactions that hinder the performance of the battery: corrosion and passivation. Corrosion consumes a large part of the silicon without contributing to the discharge. Passivation creates an oxide layer on the surface of the silicon electrode, stopping the discharge reaction. Both these reactions have been implemented in the model. Besides that, a metal contact on the silicon anode is implemented in the model. The parameters used in this model are supported by empirical values for these parameters. Finally, the model was compared to experimental results.

The simulation of the discharge of the alkaline silicon-air battery was improved in several ways compared to the pre-existing model. The corrosion was shown in the simulations, although the mechanism is somewhat simplified because of the 1D nature of the model. The passivation reaction was shown in the simulations as well, and was improved on compared to the previous model by breaking it up into two steps. Using this model, experimentally observed trends could be simulated reasonably well. The simulated discharge potential was a close representation of the experimental data, although the open circuit potential was somewhat higher, and for higher current densities the potential was somewhat lower. For different electrolyte concentrations the model showed results similar to what was found in experiments.

(This page would be intentionally left blank if the author would not wish to inform about that)

Contents

List of Figures

1

Introduction

It is generally accepted that in order to reach the goals set in the Paris agreement from 2015, an energy transition towards renewable energy sources is inevitable. If no measures are taken, the environmental impact of climate change, e.g. the sea level rise, will render large parts of the world uninhabitable. Furthermore, according to the World Health Organisation climate change is expected to have a substantial adverse effect on worldwide mortality, making health an additional reason to mitigate climate change [1]. The Paris agreement aims to reduce the emissions of green house gasses to limit the worldwide temperature rise well below 2 °C by 2050 [2].

The binding nature of the agreement has already created incentives for governmental bodies to invest in renewable sources of energy. In the Netherlands this has lead to policy changes that will promote the introduction of renewable energy sources [3]. In 2019 the share of renewable energy sources in the Dutch energy mix increased from 7.4 % to 8.7% [4]. In 2019, a significant part of the renewable energy consumed in the Netherlands came from wind- and solar energy and the latter is responsible for a significant part of the increase in 2019. According to the *Centraal Bureau voor de Statistiek* (Dutch Statistics Office), the total installed capacity of PV has increased by approximately 40% each year between 2011 and 2020. Given that the share of renewable energy sources does not yet meet the target value, the share of solar and wind energy will have to increase further in the years to come, in addition to large increases in energy efficiency [5].

In Figure 1.1 the (expected) development of the energy mix of the Netherlands between 2000 and 2030 is shown. In contrast to most fossil fuel based energy sources, many renewable energy sources fluctuate because of uncontrollable environmental conditions. For example, wind power is highly dependent on the actual wind speed, and the output of PV power is highly dependent on the irradiation. Higher penetration of these fluctuating energy sources, such as wind and solar, will lead to a need to balance energy production and demand, both on the scale of hours in the day and on the scale of seasons. Demand response will play a role in this, but shifting energy from periods of overproduction to periods of underproduction will be inevitable as well [6]. For this energy storage is needed. There are many forms of energy storage, ranging from mechanical energy storage to chemical storage in synthetic fuels and batteries. This study will revolve around one storage technology in particular: silicon-air batteries.

1.1. The necessity of energy storage

There are numerous technologies that can harvest energy with little to no carbon emissions, but often they come with variation in the output. These are so called intermittent energy sources. Intuitively one will recognize that the electricity available from photovoltaic systems and from wind-driven energy sources will vary significantly over time. One way to overcome this issue is by storing energy during periods of high production and low demand that can then be used during periods of low production and high demand. In the following paragraphs the necessity of storage will be highlighted.

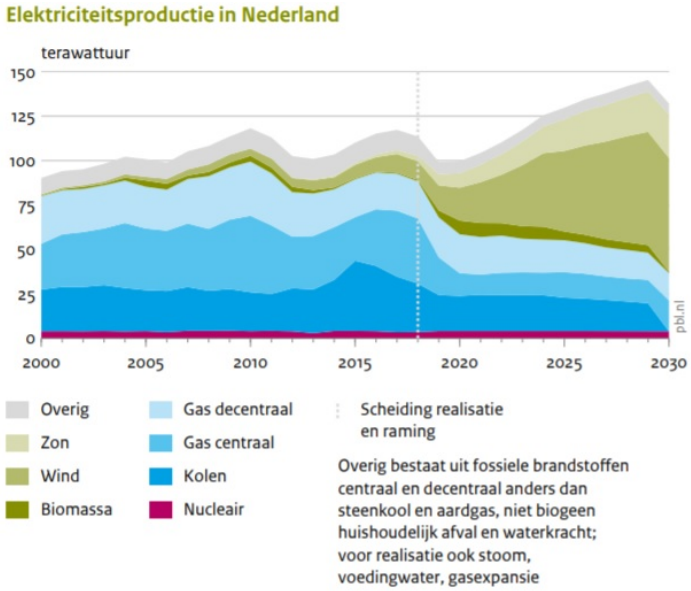

Figure 1.1: The electrical energy-mix of the Netherlands in terrawatthour from 2000 till 2030 [7].

During the day, the amount of energy harvested from solar- and wind energy sources will vary significantly. During the night there will be no power production from solar and during the day the amount of power produced will vary significantly with the altitude of the sun and with the variations in overcast. Furthermore, during the winter the amount of available sun hours is significantly less than in summer. As the seasons change, the amount of windy days and average wind speeds will change as well. In the winter there is generally more wind than during the summer [8]. Additionally, the amount of wind will change during the day from little to no wind during the morning, to a peak in wind speeds around the end of the afternoon [9].

Just like the production of energy, the demand for energy varies throughout the day. Typically the peak in demand for energy does not coincide with the peak in solar and wind production. Especially in households the demand for electricity varies throughout the day. The times when people prepare food, the times when people wash themselves, the times when people do their laundry and watch television are all linked to moments when they are home. Therefore, a clear peak in household electricity demand can be observed in the morning and evening, associated to cooking and washing [10].

Additionally, the high uncertainties in wind and solar energy make the prices quite volatile. For instance, when in the day-ahead market the amount of available wind energy is forecasted to be higher than the actual available wind energy, this will lead to price increases of electricity. On the other hand, more available wind energy than predicted can lead to price drops, and even negative prices for electricity when demand is lower than supply [11].

There are instances when there is an abundance of energy available in the electricity grid, and there are moments in time where there is a shortage. Part of this problem can be solved by a shifting loads to times where there is high availability of electricity. However, there are many cases where the load cannot be shifted. For instance, when there is no wind, nor sun during a stretch of time during the evening, the demand by households cannot be completely curtailed. To shift part of the overproduction during the day to periods where there is little to no production, this energy needs to be stored for some time [9].

1.2. Storage technologies

There are multiple technologies that can be used to store harvested electrical energy to be used at a later time. In general there are several forms of energy, one of them being electrical energy which cannot be stored as is. Therefore, the electrical energy needs to be converted into another form of

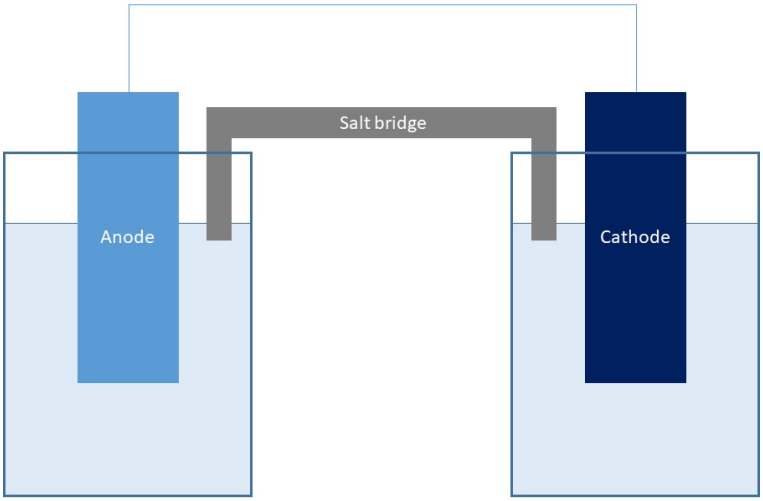

Figure 1.2: A simplified diagram of a galvanic cell.

energy, most notable chemical energy and mechanical energy. An example of the latter is pumped-storage hydro-energy. Examples of chemical storage are hydrogen fuel, synthetic fuels and batteries. This report focuses on battery storage.

1.2.1. Battery storage

A battery is a device in which chemical energy is converted into electricity and used as a source of power to be used in electrical devices. Generally, a battery consists of two half-cells that are chemically separated, but electrically connected [12]. The active materials in a basic battery are the two electrodes, an anode and cathode, and an electrolyte of some sort. At the two electrodes redox half reactions take place. Redox is a combination of the words reduction and oxidation, and hence, on the anode an oxidation reaction occurs, and on the cathode a reduction reaction takes place. When a battery is discharged, negatively charged electrons are separated from the material by the reduction at the anode and these move to the cathode where they are used in the oxidation half reaction. To compensate for this charge transfer, positively charged ions move in the same direction through the electrolyte, or through a saltbridge as is the case in Figure 1.2.

When comparing different battery types, two quite similar terms are used generously to indicate two quite different things: specific energy and energy density. The specific energy is defined as the amount of energy per mass, in this context generally given in $Wh \cdot kg^{-1}$. Energy density, is defined as the amount of energy per volume, in the context of batteries generally given as $Wh \cdot m^{-3}$.

Many different types of batteries are being developed or already exist on the market today [13]. Developments are mostly centered around increasing the efficiency and capacity of battery systems, and decreasing the cost. Common batteries are for example Lead Acid batteries, Nickel Metal Hydride batteries (NiMH) and Nickel Cadmium batteries. Especially the lithium-ion batteries (LIBs) have gained significant ground recently with their high capacity and modular application in electric cars. Older car batteries from car manufacturers have also found their way to residential applications. They have already proven in 2016 to be an economically viable solution in combination with a PV system [14]. Even if the economic incentives are disputed, the advantages for residential areas where grid failures are common often justify the investment [15].

1.2.2. Occurrence of materials for state-of-the-art lithium-ion batteries

Many of the battery technologies discussed in the previous section rely on a wide variety of materials or elements to function properly. In this section the different materials used in batteries are discussed, with a widely applied state of the art technology of this time as example: the lithium-ion battery.

Lithium-ion batteries are currently used in many different applications, ranging from laptops and mobile

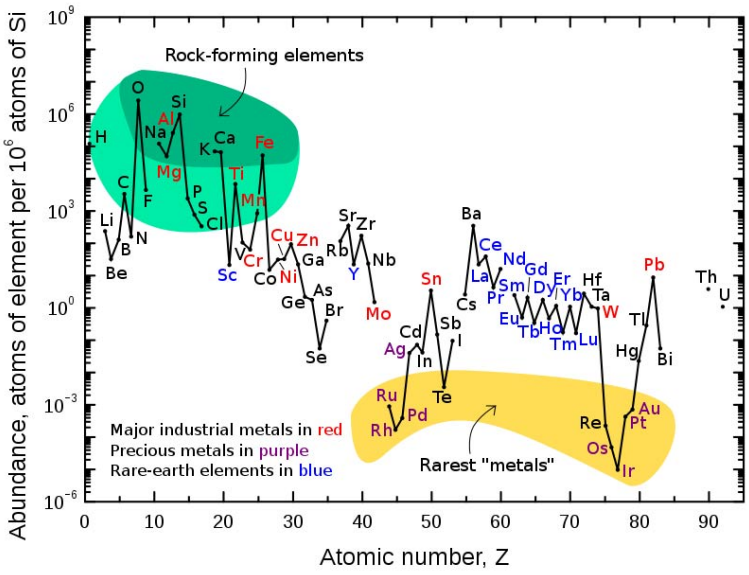

Figure 1.3: Estimate of the abundance of elements in the Earth's crust[20].

phones, to battery electric vehicles (BEVs). This is mainly due to their relatively high capacity and relatively low costs [16]. According to data of the Centraal Bureau voor de Statistiek (Dutch Statistics Office) the market share of BEVs in the Netherlands has increased massively in the last decade [17]. Economic incentives have helped in this as well and it is expected that these incentives will stay in place and further increase the market share of BEVs [18].

However, there is a significant drawback to the composition of lithium-ion batteries: they largely consist of lithium, cobalt and rare-earth elements. As can be seen in Figure 1.3 lithium, cobalt and rare-earth elements are not necessarily very scarce (silver and gold are far more "rare"), but they are difficult to extract and often are found in intricate structures with many different types of rare-earth elements [19].

Over 65 % of the worldwide supply of Cobalt comes from the Democratic Republic of Congo (DRC) [21]. Most of its raw cobalt ore was refined in China, giving Chinese industry a strategic advantage over European and US industries [22].There is strong evidence that a substantial part (15-20%) of Cobalt in the DRC is mined artisinally [23]. Given the little control and regulation there is on artisinal mines, health and safety risks are common in these mines. There is also strong evidence that there is significant child labour in these artisinal mines [24]. The artisinal extraction of cobalt may cause toxic harm to vulnerable communities in the region[25]. This means that the current supply chain of cobalt is considered unsustainable.

Because of its importance in battery technologies, lithium is listed as one of the critical minerals by the USGS [26]. It is listed as one of 29 critical elements for green technologies. At the moment of writing, the largest producers of lithium are Chile and Australia. Most lithium is mined from brine's, but these resources are scarce, and hence, lithium is a scarce and critical element.

Given the above mentioned issues with resources of lithium-ion batteries, the sustainability of these batteries can be considered questionable, especially in the long run. Alternative storage technologies with more abundant elements, such as silicon and oxygen, might provide an answer to this problem.

1.3. Research Objectives

Given the resource specific problems in many battery technologies, and the projected increase in need for storage technologies, a resource efficient technology with high capacity can provide an alternative. One of these technologies is the silicon-air battery (Si-air battery), a specific type of Metal-air batteries. It has been investigated extensively by among others Weinrich and Durmus from the Institute of Energy

and Climate Research-Fundamental Electrochemistry (IEK-9) in Jülich(Germany) [27, 28], and Cohn and Ein-Eli from the Department of Materials Engineering at Technion-Israel Institute of Technology in Haifa [29, 30] . Many other papers on silicon-air batteries have been published by several other research institutes in the last decade.

Besides the abundance of silicon and Oxygen in the Earth's crust pointed out in Figure 1.3, silicon-air batteries have a high theoretical specific energy (8470 Wh/kg, this will be further discussed in Section 2.1). However, in previous research two specific issues have been identified that dramatically decrease this specific energy and lifetime of silicon-air batteries. Firstly, there is significant **corrosion** of the silicon anode, limiting the amount of silicon that is effectively used in the oxidative discharge to a fraction of the total consumed in the anode, with a mass conversion efficiency ranging from 2% to 6% reported by Durmus et al. [31].

The second evident issue in discharging silicon-air batteries for longer periods is the building of a **passivating** Oxide layer. This passivation affects both the air electrode, and the silicon electrode.

The objective of this research is:

To develop a digital model in finite element modeling of the passivation, corrosion and discharge in silicon-air batteries.

In the next chapter the silicon-air battery is discussed in detail. The passivation and corrosion mechanisms are discussed. In the third chapter the experimental methods are discussed, followed by the results that followed from the conducted experiments in the fourth chapter. In the fifth chapter the Finite Element Model is discussed, followed by the results obtained from the model in Chapter 6. The results are then discussed and concluded in Chapters 7 and 8. followed by an outlook and recommendations.

2

Alkaline silicon-air batteries

An alternative to the more commonly known battery technologies briefly discussed in Section 1.2.1 is the silicon-air battery. As the name already suggests, the battery consists of a silicon electrode and an air electrode [30, 32]. The general chemistry and some characteristics of the silicon-air battery are discussed in this section.

2.1. Metal-air batteries

When discussing metal-air batteries, a specific group of batteries consisting of a metal electrode and an ”air” electrode is meant. The metal electrode can be made from different metal species, for example Zn or Al. The air electrode is generally an oxide transporting membrane of some sort. This allows for atmospheric oxygen to pass through to the electrolyte where it can react. Given that the oxygen is taken from the air, there is no need for a second (heavy) metallic electrode. This allows for a significant reduction in weight and cost of the battery, and hence an increased specific energy in $Wh \cdot kg^{-1}$. In almost all metal-air batteries, the metal electrode is directly used in the electrochemical discharge reaction. This means, contrary to for example lithium-ion batteries, that there are no other elements needed for the metal electrode than the metal itself, further increasing the specific energy. The specific energy and energy density of several metal-air couples are shown in Figure 2.1. This figure shows that lithium-air, aluminium-air and silicon-air are especially interesting couples [33].

In addition to the performance gains, the metals used for the metal electrodes in metal-air batteries are generally relatively abundant. Rare or hard to come by elements such as cobalt or rare-earth elements are not needed. An especially interesting battery type from this perspective is the silicon-air battery [28]. One might not consider this a metal-air battery as silicon is a semiconductor, and hence the name ”Semiconductor-air” battery might be more appropriate. Nevertheless, in literature it is generally considered a metal-air battery, as the general principle is quite similar.

2.2. Materials used in silicon-air batteries

As discussed in Section 1.2.1 most modern battery technologies rely on the use of rare-earth elements, materials from questionable sources such as cobalt or materials that can cause significant end-of-life pollution. As will be discussed in Section 2.3 the chemistry of the silicon-air battery discussed in this study relies on silicon for the anode, hydroxide as electrolyte, and zinc for the air cathode. As highlighted by Weinrich et al.[28], silicon is one of the most abundant materials on earth. Given the abundance, silicon-air batteries provide an interesting and resource efficient alternative for other battery technologies. Besides the high availability of silicon and oxygen, the silicon/oxygen couple potentially provides high volumetric- and gravimetric energy density. Cohn et al.[30] reported a theoretical specific energy of 8470 $Wh \cdot kg^{-1}$.

The silicon used in the anode is often doped crystaline silicon. This implies there will be other elements in the silicon, such as boron, aluminium, or gallium for p-type silicon, or nitrogen, phosphor, or arsenic

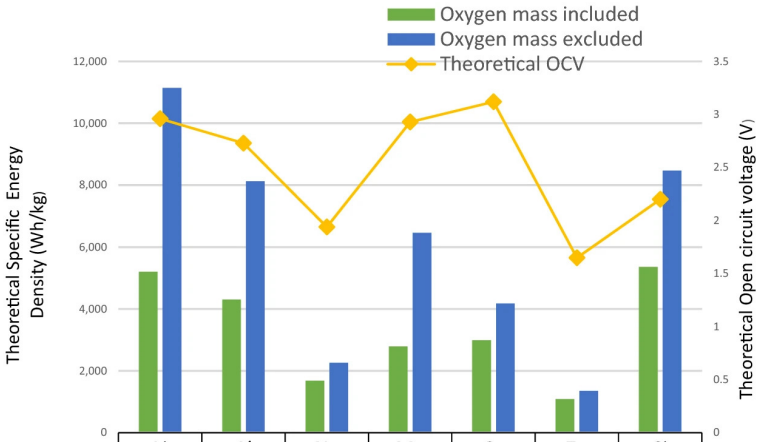

	Li	Al	Na	Mg	Ca	Zn	Si
Oxygen mass included	5,200	4,300	1,677	2,789	2,990	1,090	5,360
Oxygen mass excluded	11,140	8,130	2,260	6,462	4,180	1,350	8,470
Theoretical OCV	2.96	2.73	1.94	2.93	3.12	1.65	2.2

Figure 2.1: Theoretical energy densities of different types of metal-air batteries. The theoretical OCV is the theoretical open circuit potential of the metal-oxygen combination and is plotted in yellow. The energy density including and excluding oxygen are plotted in green and blue respectively. From Bansal et al. [34] and based on Kraytsberg et al.[35].

for n-type doped silicon. The active material on the cathodic side during discharge is atmospheric oxygen. Generally speaking, the air-electrode consists of a metallic mesh with active carbon contained in the pores of the mesh. This ensures a proper diffusion of oxygen into the battery and simultaneously contains the electrolyte.

As discussed in Section 1.2.2 many current battery technologies rely on scarce by elements from sometimes disputable sources. This opens up the interest for more resource-efficient battery technologies. The sheer abundance of silicon and oxygen (as shown in Figure 1.3) makes the silicon-air Battery a very interesting proposition.

2.3. Chemistry of silicon-air batteries

An alkaline silicon-air battery consists of an air cathode, silicon anode and alkaline electrolyte. The system relies on an anode/cathode couple, silicon in the anode and oxygen from the air in this case.

The silicon anode is consumed in the anodic half-cell reaction described in Equation 2.1. In the cathodic half-cell reaction described in equatoion 2.2 the oxygen from the air reacts with the electrolyte at the cathode. The cathode consists of manganese based catalyzed carbon and as shown in Equation 2.3 is not consumed in the primary discharge reaction [36].

The discharge (half)reactions that take place in the battery are given below [30][32]. Figure 2.2 gives a visual representation of the discharge half reactions.

At the anode:

$$Si + 4\,OH^- \longrightarrow Si(OH)_4 + 4\,e^- \tag{2.1}$$

At the cathode:

$$O_2 + 2\,H_2O + 4\,e^- \longrightarrow 4\,OH^- \tag{2.2}$$

The overall discharge reaction is:

$$Si + O_2 + 2\,H_2O \longrightarrow Si(OH)_4 \tag{2.3}$$

One can notice in Equation 2.3 that the only elements consumed in the discharge reaction are water, oxygen and most importantly, silicon. These elements form $Si(OH)_4$ which is to some extent soluble

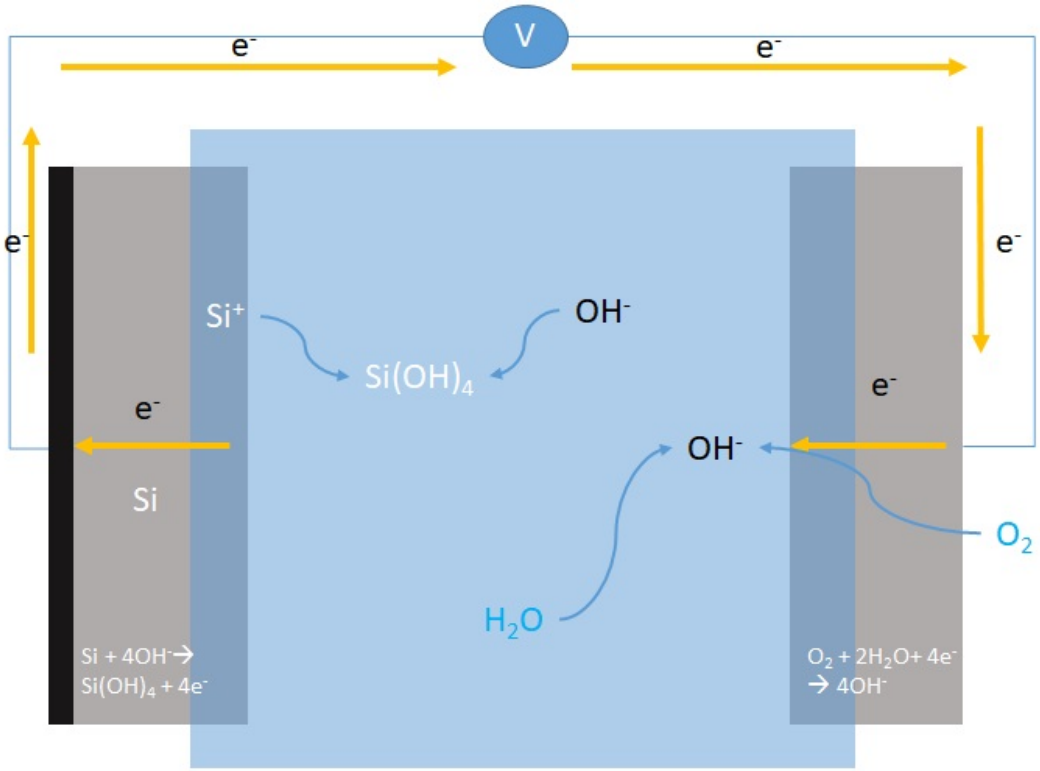

Figure 2.2: A schematic representation of the discharge of an aqueous alkaline silicon-air Battery with the anodic and cathodic half reactions during discharge.

in the alkaline electrolyte. As is pointed out by Zhong et al. [32], in the case of a flat silicon wafer this reaction product needs to be removed from the anode promptly, as the $Si(OH)_4$ can build up on the surface of the anode. This will then lead to the formation of a layer of SiO_2 on the anode surface, essentially passivating the anode and stopping the battery operation. In the research by Zhong et al [32]. the formation of $Si(OH)_4$ was found to be 50-100 times larger than the dissolution of SiO_2. Wafers with increased porosity, effectively increasing the surface area, were found to have increased dissolution rates, effectively etching away the passivation layer [32]. This means that a larger part of the anode can be consumed and the battery can be discharged for a longer time. According to Prins [37], the lifetime can be further improved on the cathode side by prewetting the air cathode in an alkaline solution. The prewetting had a positive impact on the cathode because of two reasons. The presence of OH^- provided more oxygen reduction. Secondly, the increased micropore area provided additional surface area, reducing the suffocation effect by other atmospheric gasses.

The practical Open Circuit Potential (OCP) and discharge potential depend on the dopant type in the silicon anode and the concentration of the electrolyte. Durmus et al. [31] have shown that As-doped silicon provides the highest potential. However, as shall be discussed in more detail in Section 2.5, this dopant also results in the highest corrosion rate. The potential of the silicon-air battery increases for concentrations of electrolyte higher than 2M. Up to 1M the discharge potential was around 1.1V. For concentrations of 2M 1.2V was observed and this increases slightly for even higher concentrations, to 1.27 at 5M. This attributed to the increased electrolyte conductivity and lower overpotentials due to faster reaction kinetics [27].

2.4. Passivation in silicon-air Batteries

As indicated in the introduction to this thesis, passivation in the silicon-air battery has been indicated in litereature as one of two main limiting factors in silicon-air batteries [29, 32, 38]. During discharge $Si(OH)_4$ (silicic acid) is formed, as shown in figue 2.3. The silicic acid is dissolved in the electrolyte. However, the amount of silicic acid that can be dissolved in an alkaline electrolyte is limited and the

dissolution happens at a limited rate. When the rate of dissolution of the reaction product becomes less than the rate of formation of the silicon oxide, or the limit of silicic acid dissolved in the electrolyte is reached, the $Si(OH)_4$ starts to split into a silicon oxide and water. The chemical equation of this oxide formation is shown in Equation 2.4.

$$Si(OH)_4 \longrightarrow SiO_2 + H_2O \tag{2.4}$$

The silicon oxide is a solid and dissolves into the electrolyte at quite a low rate. Furthermore, the formed oxide is very stable in aqueous envrironments, as will be discussed further in 2.5.1 Section [39]. Therefore, a silicon oxide layer deposits on both electrodes, effectively passivating the electrode surfaces and preventing the discharge reaction. A schematic representation of the formation of this passivating layer is shown in Figure 2.3.

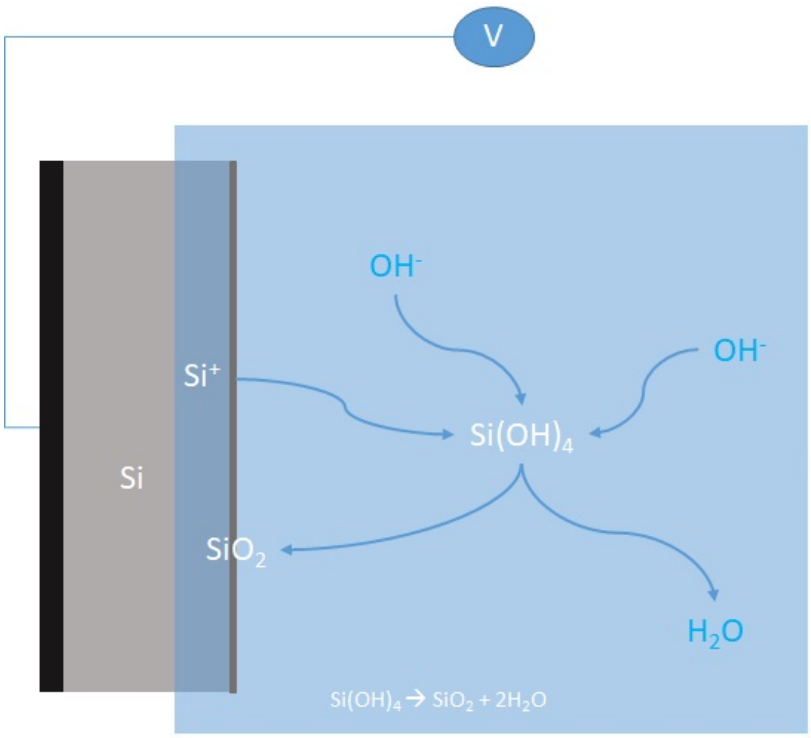

Figure 2.3: A schematic representation of the passivation of the anode in aqueous alkaline Si-air batteries

Accordig to Cohn et al. [29] the way in which the pores of the air electrode are clogged by the buildup of silicon oxide in the air electrode depends strongly on the discharge current in the battery. This is shown in Figure 2.4. Note that in this specific case a non-aqueous electrolyte was used.

According to Palik et al. [40] when crystalline silicon is etched in an alkaline solution the formed passivating layer is a suboxide layer. This means that instead of SiO_2 a form with less oxygen is formed, SiO_x with $0 \leq x \leq 2$. Eventually this suboxide can react further to eventually form SiO_2. This suboxide has significant impact for the passivating behavior of the silicon oxide as the suboxide can conduct electricity to some extend, with reported conductance of $6.7 \cdot 10^{-4}$ $S \cdot cm^{-1}$ [41]. With a conductance in the order of 10^{-12} $S \cdot cm^{-1}$ [42] SiO_2 is a good insulator. This implies that when the oxide layer is formed on the anode, this is likely to start of as some suboxide.

Several solutions for the passivation have been suggested. When examining the anode in detail, there are several parameters impacting the passivation significantly that possibly can be tweaked. First, the surface area on which the passivating layer is deposited. If a larger area is available for contact with the electrolyte to continue the discharge, it will increase the time needed to fully passivate the active surface area. Surface texturing may provide a solution to this.

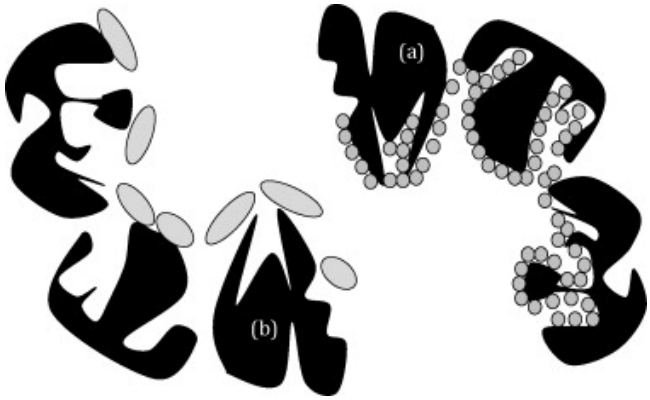

Figure 2.4: The clogging of pores in the air electrode by SiO_2 in the passivation reaction of a non-aqueous silicon-air battery. (image taken from [29])

2.5. Corrosion in silicon-air batteries

The second significant limiting factors in the further development of silicon air batteries is the corrosion reaction that takes place on the anode. The corrosion reaction is a parasitic reaction that can consume a significant portion of the silicon in the anode. [27] First, the mechanism of corrosion is described. Second, the influence of the wafer on the corrosion is described. Last, the effect of electrolyte concentration and battery potential on corrosion are discussed.

2.5.1. The corrosion mechanism

In the corrosion reaction, the electrons are not transported to the current collector. Instead, the electrons are moved to so called cathodic sites where they react with water. This forms hydroxide and hydrogen gas. Meanwhile $SiO_2(OH)_2^{2-}$ is formed by a reaction of the silicic acid and hydroxide [28, 37].

The partial corrosion reactions of the silicon in alkaline environment are given below. Note that this whole process takes place locally at the anode surface [28].

Anodic sites:

$$Si + OH^- \longrightarrow Si(OH)_4 + 4\,e^- \tag{2.5}$$

Cathodic Sites:

$$4\,H_2O + 4\,e^- \longrightarrow 4\,OH^- + 2\,H_2 \tag{2.6}$$

Bulk electrolyte:

$$Si(OH)_4 + 2\,OH^- \longrightarrow SiO_2(OH)_2^{2-} + H_2O \tag{2.7}$$

The overall corrosion reaction is:

$$Si + 2\,OH^- + 2\,H_2O \longrightarrow SiO_2(OH)_2^{2-} + 2\,H_2 \tag{2.8}$$

From Equation 2.8 it follows that silicon is consumed and dissolved at the anode, without involvement of an external circuit, and hence these electrons do not contribute to an external current. According to Durmus et al. [43], assuming the four-electron system described in Equation 2.5, this corrosion reaction reduces the mass conversion efficiency of the silicon anode to a maximum of 50%. According to literature the practical mass conversion efficiency during discharge is only around 3% [28, 31]. The corrosion rate is mainly chemical in nature, since the electrochemical contribution to the overall corrosion is found to be only 0.5%. The transfer of electrons between the electrolyte and silicon is suspected to be the limiting factor in the oxidation reaction. Furthermore, the OH^- was found to be a catalyst, and therefore the concentration had little influence in the corrosion reaction at OCV. Discharging the cells was found to have an enhancing effect on the corrosion, because of the increased flow of OH^- onto the anode surface [31]. According to Durmus et al. [43] the corrosion reaction is the major limiting factor in the further development of silicon-air battery.

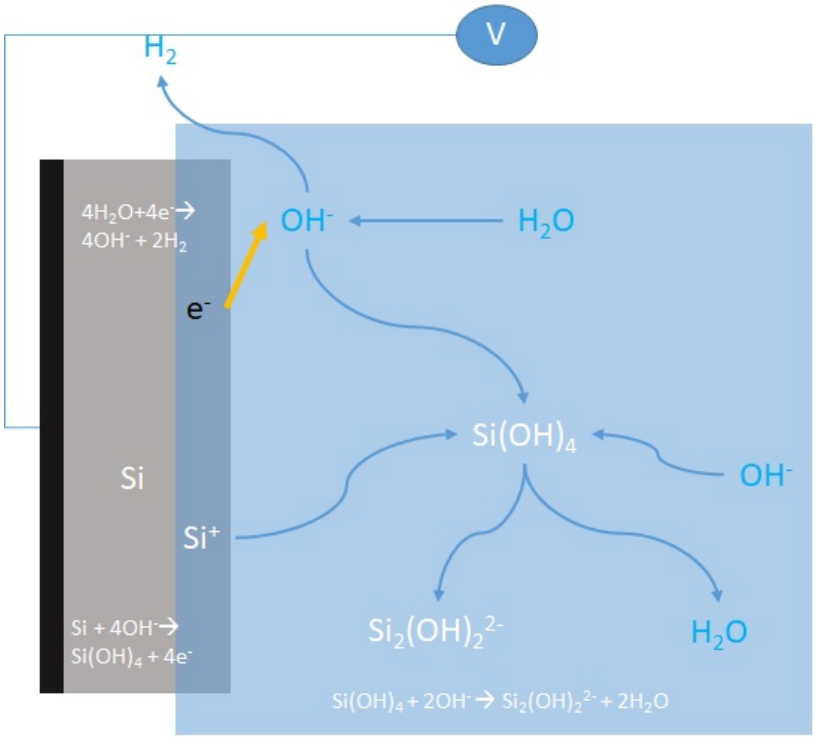

Figure 2.5: A schematic representation of the corrosion in aqueous alkaline silicon-air batteries.

The corrosion during OCV is effectively the same as etching of silicon in KOH. Etching of silicon has been studied extensively over the years, so the mechanisms behind this are quite well understood. Raley et al. [44] have proposed a model for the chemical etching of silicon in alkaline solution.The chemical reactions very closely resemble the corrosion reaction Equation 2.8. Among others, Allongue et al. [45, 46], Seidel et al. [47, 48], and Palik and Glembocki et al. [40, 49–51] studied different factors influencing the etch rate and etching mechanisms of silicon in alkaline solutions, most notably:

- Orientation dependence [46, 47, 50].
- The influence of dopants [48, 51].
- Concentration [49].
- Bias dependence [40, 45].
- Surface quality [52].

2.5.2. Potential- and electrolyte dependence

A useful tool for the analysis of the concentration dependence of the corrosion of the anode is the electrolyte stability window. This stability window can be illustrated in a so called potential-pH diagram, also called Pourbaix diagram, named after the 20th century chemist Marcel Pourbaix.
Pourbaix diagrams can be used as an electrochemical map, indicating stability domains of ions, oxides and hydroxides [53]. Figure 2.6 shows the Pourbaix diagram for water and oxygen. The horizontal axis shows the pH, and the vertical axis represents the electrical potential over the electrolyte. The lines represent the stability window of water: for potiential/pH values between these lines water is stable. As the name suggests, outside the stability region water is unstable and decomposes. Below the bottom line, the formation of H_2 is favoured, and above the top line the formation of O_2 is favoured.

Figure 2.7 shows the pourbaix diagram of silicon in aqueous solution. Again, the stability window of water is shown between the dashed lines. Evidently, when using aqueous electrolyte one will face passivation. Crystaline silicon is well outside the stability window, and hence the silicon is prone to

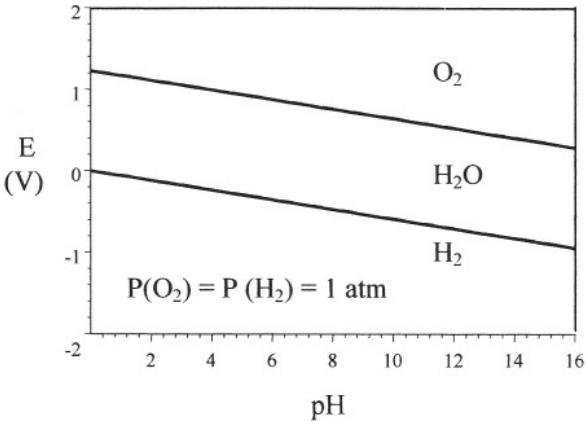

Figure 2.6: The stability window for water [53].

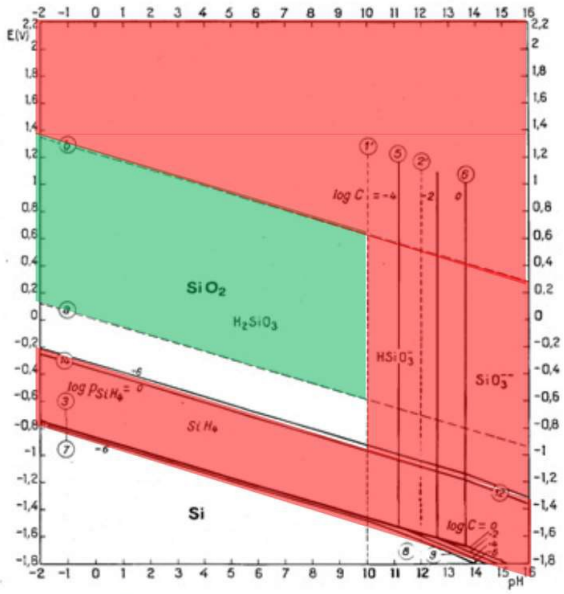

Figure 2.7: The Pourbaix diagram for silicon in an aqueous electrolyte. The red area represents corrosion and the green area represents passivation (which was discussed in more detail in 2.4) (Image taken from [37], based on [53] and [54]).

instant oxidation [28].

Within the window where corrosion takes place, the rate of corrosion will differ. For increasing concentration of OH^- the corrosion rate will increase to a certain level. For the corrosion of silicon both water and hydroxide ions are needed [49]. For increasingly high pH, OH^- concentration will increase. However, simultaneously there will be relatively less water due to hydration effects. This produces a peak in the corrosion rate as a function of pH.

As shown by the Pourbaix diagram, the pH and potential applied to the battery both have significant influence on the corrosion rate. Whereas the potential is generally a given in the battery, because of the halfcell potentials, the pH can be altered to get to the desired discharge and corrosion.

2.5.3. Influence of silicon wafer specifications

The corrosion rate of the crystalline silicon is influenced significantly by the orientation of the crystal lattice and on the doping of the wafer. This has been shown to apply in silicon-air batteries as well [29]. An overview of the corrosion rates for different silicon wafers is shown in Figure 2.8.

When etching a silicon wafer the different surface orientations have different etching rates. The investigated crystal orientations in crystalline silicon are <100>, <110> and <111>.

2.6. Rechargeable silicon-air batteries

One of the biggest advantages of lithium-Ion batteries is the large cycle life. The silicon-air battery described so far is a primary battery and for it to be an alternative to the state-of-the-art lithium-ion batteries, a rechargeable silicon-air battery is required. However, a stable oxide is formed in the discharge and passivisation reactions, as discussed in 2.4 [39]. This means that reversing the discharge reaction can only be done under specific conditions.

However, Inoishi et al. [55] have reported a rechargeable silicon-air solid-state oxygen shuttle battery with an oxide-ion conductor. In this case the electrolyte is a solid oxide ion conducting electrolyte, from ZrO_2, stabilized with CaO. A schematic representation of this cell is shown in Figure 2.9. This cell was capable of 20 stable charge-discharge cycles with an average capacity of 600 mAh $\cdot g^{-1}$. One of the

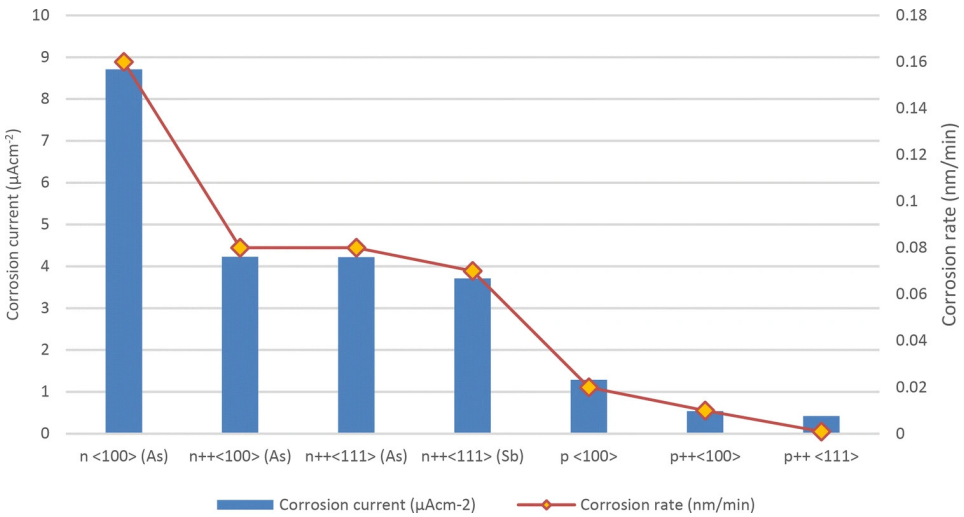

Figure 2.8: The corrosion rate in silicon-air batteries for different dopants and different crystal orientations. Graph courtesy of Bansal et al. [34] based on the work by Cohn and Ein-Eli [29].

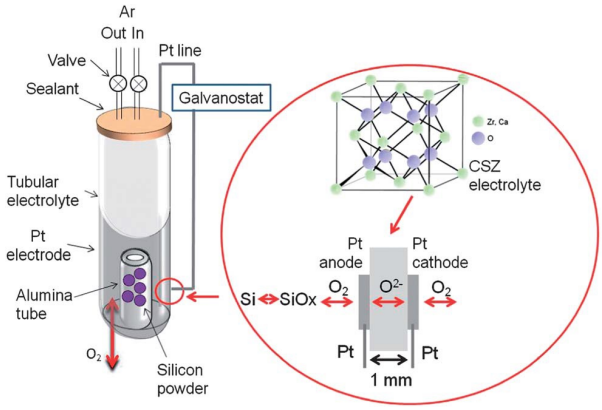

Figure 2.9: Schematic representation of the experimental setup of a rechargeable silicon-air cell with Ca stabilized ZrO_2.

drawbacks of this concept is the operating temperature, as the battery was cycled at 1073 K. Also, the round trip efficiency of 45% was quite low when compared to more common rechargeable batteries such as Li-ion batteries. Furthermore, the platinum used in the cell does not exhibit the ideal level of catalytic activity for the oxygen reduction.

The illustrated concept is an interesting preliminary attempt of finding rechargeable silicon-air batteries. It has proven to be an actual rechargeable battery. However, it requires a further increase in performance, as the operating temperature is too high and the round trip efficiency is quite low.

2.7. Semiconductors

Generally speaking, metals have high conductivity and insulators have low conductivity. This means that metals can transport currents significantly better than insulators. However, there is a group of materials that is somewhere in between the two: so-called semiconductors. These materials form the basis for integrated circuits that are the basis of most modern communication devices [56]. In this chapter the basic principles of semiconductors that are relevant to this research are discussed.

2.7.1. Doping, energy levels and energy band diagrams

All elements consist of a number protons and electrons. Protons are positively charged particles in the nucleus of an atom and electrons orbit this nucleus. Silicon is the 14th element, and this means that

silicon has 14 electrons in neutral state. The electrons orbit in different shells around the nucleus. The first shell holds two electrons. The second shell holds 8 more. This brings the total to 10 electrons, hence there are four more electrons in the third shell. These outermost electrons can form chemical bonds and are called *valence electrons*. Two atoms form a covalant bond when they share a valence electron. Given that there are four valence electrons, silicon atoms can form four chemical bonds [56].

A number of silicon atoms that are bonded together form a crystal lattice. At normal operating temperature (300K), some of the lattice bonds are broken, freeing some of the valence electrons. These free electrons are free to to move around the lattice and can therefore conduct electricity. The place that is left behind by the electron, that can be regarded as positively charged, is called a *hole* [57]. A valence electron of a neighboring atom can then jump into this hole. In practice the crystal lattice will always contain some imperfections, such as broken bonds or impurity atoms. If the number of impurity atoms is low, this is referred to as an *intrinsic semiconductor*.

The concentration of the electrons and holes can be manipulated by introducing impurities to the crystal lattice. Some silicon atoms are replaced by atoms with either three valence electrons, such as boron, or five valence electrons, like phosphorus. This is called *doping* [57]. When a silicon atom is replaced by a phosphorus atom, four of the valence electrons will restore a bond with the surrounding silicon atoms, but the fifth valence electron cannot form a bond. This electron stays weekly bound to the phosphorus atom, but is easily liberated from the atom to then become a free electron. In this way, the introduced phosphorus donates an electron, and therefore atoms that increase the number of free electrons are called *donors*. A semiconductor that is doped with donors is called *n-type*. In the case of boron, there are only three available valence electrons, and therefore the fourth valence bond is not formed, effectively creating a hole where it can accept an electron from the lattice. These doping elements are called *acceptors*. A semiconductor that is doped with acceptors is called *p-type*. The amount of available holes or available electrons is the carrier concentration. The carrier concentration of a semi conductor has a significant influence on its conductivity. The possibility of tweaking the carrier concentration with doping is a very useful feature of semiconductors.

The *density of states* is the function of all allowed energy states of the electrons, whether they occupy a valence position, and are therefore bound to an atom or are not bound to an atom, and are in the conducting state. The Fermi-Dirac function describes the chance that an energy levels is occupied by an electron. In silicon electrons can only have discrete energy levels. Because of the periodic structure of atoms, there is a range of allowed energy levels that can be occupied by an electron. These are called energy bands. The excluded energy levels form the *band gap*. The electrons that are in chemical bonds are called valence electrons, and therefore all allowed states of valence electrons is called the *valence band* [57]. Electrons liberated from the bonds can also have only discrete energy levels, and all allowed states of these conduction electrons form the *conduction band*. The gap between the maximum level of a valence electron, E_v, and the minimal energy level of a conduction electron, E_c is the band

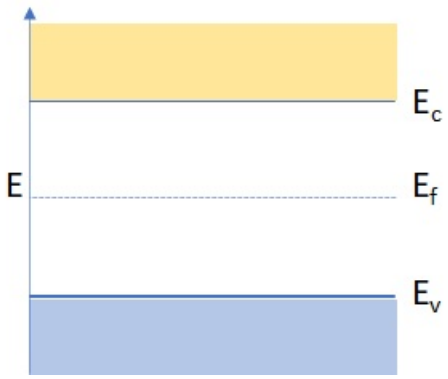

Figure 2.10: An energy band diagram for an intrinsic semiconductor. The conduction band is shown in yellow, and the valence band is shown in blue. The average energy level is the Fermi level, E_f. In this case E_f is located in the middle of the bandgap, as this is the band diagram for a semiconductor that is not doped.

gap. The effective average level of all electrons in the lattice is the Fermi level. These energy levels can be visualised in an energy band diagram, such as Figure 2.10.

The average level of electrons will change for different doping levels. An n-type semiconductor will have more free electrons, and therefore the Fermi level level will be closer to the conduction band. A p-type semiconductor will have few free electrons and therefore the fermi level will be closer to the valence band. The exact position of the Fermi level as function of the impurity concentration can be calculated using:

$$E_c - E_f = k_b T \ln\left(\frac{N_c}{N_D}\right) \tag{2.9}$$

$$E_f - E_v = k_b T \ln\left(\frac{N_v}{N_A}\right) \tag{2.10}$$

E_c, E_f and E_v are the bottom of the conduction band, the Fermi level and the top of the valence band respectively in eV. T is the temperature in K and k_b is the Boltzman constant in given in J·K^{-1} or in eV·K^{-1} that links temperature to energy. N_c, N_D, N_v and N_A are the effective density of states in the conduction band, the donor concentration, the effective density of states in the valence band and the acceptor concentration, respectively, in cm^{-3}.

2.7.2. Metal-semiconductor contact

As discussed, the level of the Fermi level in semiconductors depends on the doping of the semiconductor. Metals are generally considered conductors. The contact between a metal and a semiconductor can in some cases lead to a so-called Schottky barrier. This will be discussed in this section.

In the band diagram of a some metal a band is partially filled, which means that the Fermi energy is in the middle of this band. For other metals there is an overlap between the conduction band and the valence band. An important parameter is the work function, ϕ_m. This describes the required energy to remove an electron from the Fermi level to a position outside the material, the vacuum level. Semiconductors also have a work function, ϕ_s in this case. Besides this, electrons in semiconductors also have an electron affinity, χ, which represents the energy difference between the vacuum level and the lower edge of the conduction band [58]. From this it follows that the difference between χ and ϕ_s is the energy difference between the conduction band and the Fermi level. This can also be defined the other way around, if the electron affinity is already known for a semiconductor:

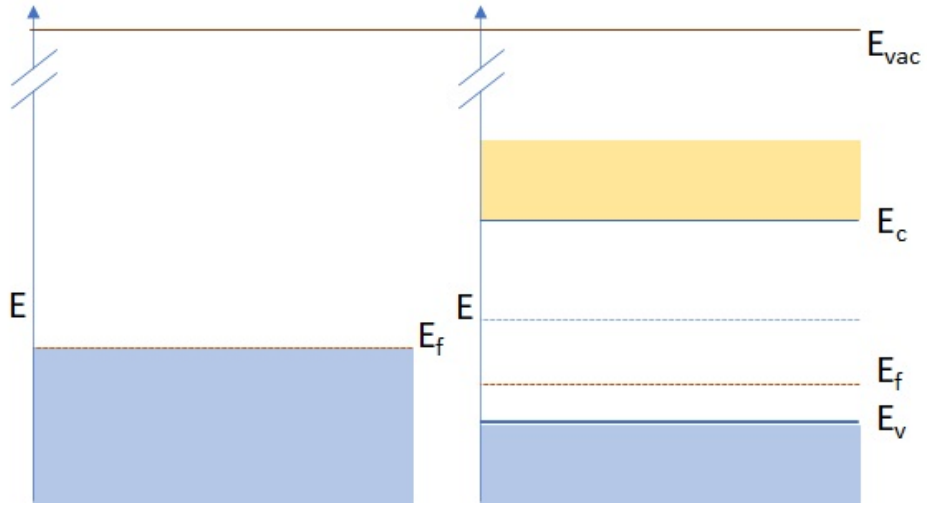

Figure 2.11: The band diagrams of a metal and a p-type semiconductor next to each other, but not in contact. In this case the vacuum levels will be aligned.

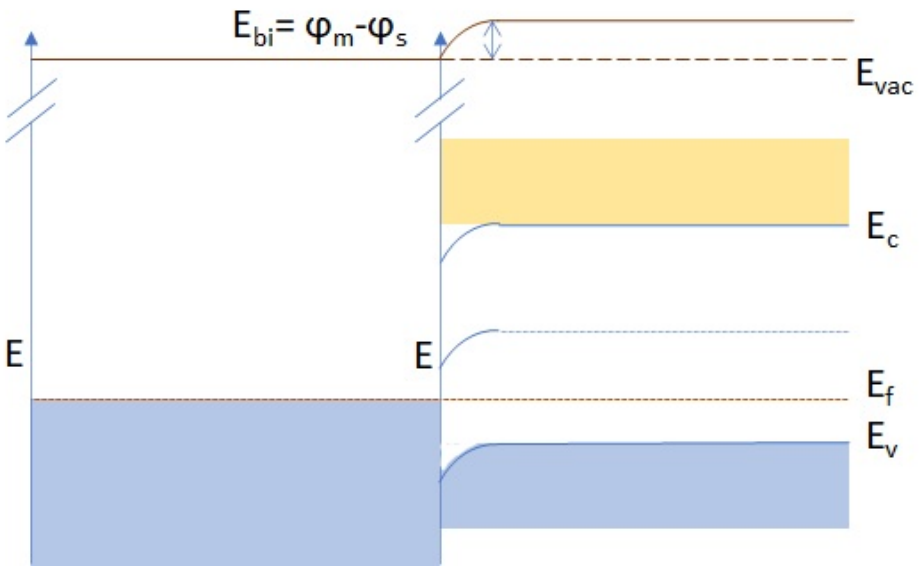

Figure 2.12: The band diagrams of a metal and a p-type semiconductor in contact. In this case the Fermi levels will be aligned and the vacuum level will be continuous, forming a Schottky barrier. This is called E_{bi}, the build in voltage.

$$\phi_s = \chi + (E_c - E_f) \tag{2.11}$$

When a metal and semiconductor are brought together, two things will happen: first, the Fermi levels will allign, and second the vacuum level will be continuous. This means that a barrier is formed [58]. This is shown in Figure 2.12. This is a so-caller Schottky barrier. In this barrier a potential drop the size of this barrier will be observed.

Different metals have different values for the metal work function. When the Fermi level of the silicon that is to be contacted is known, an appropriate metal can be chosen based on its work function, to minimize the difference in work function between the metal and the semiconductor to minimize the energy loss in the Schottky barrier.

2.8. Experimental considerations

From literature some parts can be integrated in the further proceedings of this research. These considerations are highlighted in this section.

- According to Prins [37], prewetting the air cathode will increase both the discharge potential and the discharge time. .
- As discussed by Jacob[59], as well as by Prins [37], the use of an aluminium back contact, alloyed with 1% silicon is speculated to improve the open-circuit potential.
- According to Durmus et al. [43] p-type doped silicon shows significantly lower corrosion than n-type doped silicon, but also provides lower discharge potentials.
- As the described chemical reactions at the anode of the silicon-air battery are dissolving the silicon into the electrolyte, this will lead to weight loss of the actual anode. This is also supported by literature [43] [28].
- In order to stop the corrosion reaction on the anode, the electrons that cause the reaction will need to be collected at the current collector before participating in the corrosion. In order to do so an approach with a doping profile in the anode is suggested.
- The depth, concentration and type of doping are yet to be determined.

- Cohn and Ein-Eli suggest that the use of n-type silicon potentially yields higher discharge potential than using p-type silicon, but the increase in corrosion that n-type silicon yields lower practical discharge potential [29]. This was also confirmed by Prins [37].

3

Experimental Methods

In this chapter the experiments are described. First, the considerations and reasoning for the experiments is highlighted. After this, the assembly is discussed, including descriptions of the different parts of the battery cell and chemically active parts.

3.1. Experimental motivation

In this research a test setup to discharge silicon-air batteries is required. The amount of silicon on the anode that is consumed during discharge needs to be quantified. The two systems that are considered for the consumption of silicon in the cell are the corrosion reaction and the discharge reaction. In both the corrosion and discharge the silicon is dissolved in the electrolyte and hence the amount of silicon left on the electrode is reduced. This means that there is a mass difference between the electrode before and after discharge. Based on the discharge current, the amount of silicon contributing to the discharge can be calculated. It is hypothesised by Zhong et al. [32] that the aforementioned oxidation and corrosion reaction are the only reactions consuming the silicon electrode. This means that the mass consumed by the corrosion reaction can be calculated[31].

$$m_{consumed} = \Delta m_{anode} = m_{initial} - m_{afterdischarge} \tag{3.1}$$

From the above mentioned assumptions it follows that:

$$m_{consumed} = m_{oxidation} + m_{corrosion} \tag{3.2}$$

Given that $m_{oxidation}$ can be calculated from the discharge current and $m_{consumed}$ can be determined using mass measurement, $m_{corrosion}$ can be determined from Equation3.2.

During discharge, silicon is consumed in the oxidation of the anode at a rate that is dependent on the discharge current. The mass of silicon that is consumed in this reaction and the current density are coupled in Equation 3.3.

$$m_{consumed} = \frac{JA}{n_e \cdot e} \cdot t_{discharge} \cdot \frac{\rho_{Si}}{N_{Si}} \tag{3.3}$$

Here J is the current density in [A· m^{-2}]. A is the area of the electrode in m^2. The number of electrons in the discharge reaction is n_e and has no unit. The elementary charge e is $1.602 \cdot 10^{19}$ Coulomb. The discharge time is denoted by $t_{discharge}$. The density of silicon is given as ρ_{Si}. Lastly, $N_s i$ is the atomic density of silicon.

Current density is defined as:

$$J = \frac{I}{A} \tag{3.4}$$

I is the current in A and A is the electrode surface area in m^{-2} Using the definition of current density in Equation 3.4 equation 3.3 simplifies to:

$$m_{consumed} = \frac{I \cdot t_{discharge} \cdot \rho_{Si}}{n_e \cdot e \cdot N_{Si}} \tag{3.5}$$

The discharge half reactions that take place in the battery are the following: [30][32]
At the anode:

$$Si + 4\,OH^- \longrightarrow Si(OH)_4 + 4\,e^- \tag{3.6}$$

At the cathode:

$$O_2 + 2\,H_2O + 4\,e^- \longrightarrow 4\,OH^- \tag{3.7}$$

The overall discharge reaction is:

$$Si + O_2 + 2\,H_2O \longrightarrow Si(OH)_4 \tag{3.8}$$

From the anodic halfcell reaction 3.6 it is known that for each silicon atom 4 electrons are extracted, hence n_e is 4. Furthermore, the atomic density of silicon and the mass density of silicon are known. These constants can be reduced to a single constant, c, with value 7.278 g· C^{-1}. Therefore, the mass consumed in the discharge reaction is a function of time and current, as shown in 3.9.

$$m_{consumed} = c \cdot t_{discharge} \cdot I_{discharge} \tag{3.9}$$

If the experiments are conducted at constant current, a so-called galvanostatic experiment, the amount of silicon consumed in the discharge reaction increases linearly.

3.2. Cell design

For the experiments in this research a custom cell was designed and manufactured. The purpose of this cell is to hold the electrodes and the electrolyte, and to provide a connection to an external circuit. The cell consists of three separate 3D printed blocks. The central block is designed to hold the electrolyte. There is a hole in the top of this block to allow for electrolyte to be poured into the cell after assembly of the cell. The two outer blocks are designed to create a sealed connection between the electrolyte and the electrodes and to provide an electrical contact on the electrode's backside. The holes through which the wires run also allow the flow of oxygen in the air to the air cathode. The openings where the electrolyte and electrode meet have a surface of 1 cm^2, therefore the active area for each experiment is 1 cm^2. This yields that obtained results can be compared to literature with simple and straight forward area expressions.

The electrolyte is an alkaline solution and therefore the cell is made of polytetrafluoretheen (PTFE) better known by its brand name Teflon. This plastic is resistant to alkaline solutions. The seal between cell and electrode is further improved with PTFE O-rings. This ensures a near perfect seal. Nevertheless some leakage was observed during some of the experiments when the assembly was slightly misaligned.

The contacts consist of a contact plate, a spring and a wire soldered to the spring. This wire is easily connected to the measurement equipment using crocodile clips on the measurement cables. The

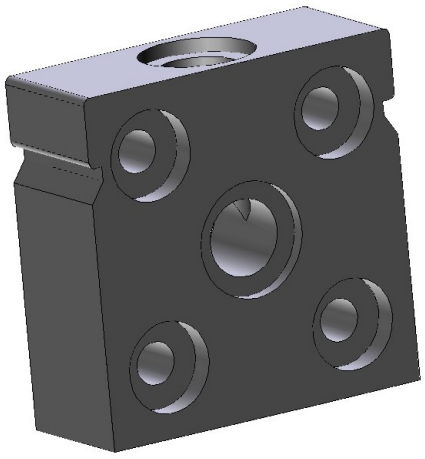

Figure 3.1: Central part of the cell

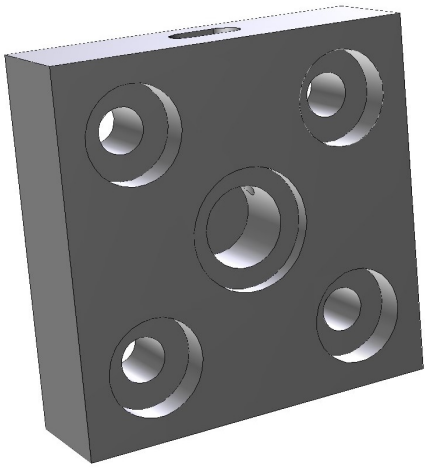

Figure 3.2: Outer parts of the cell

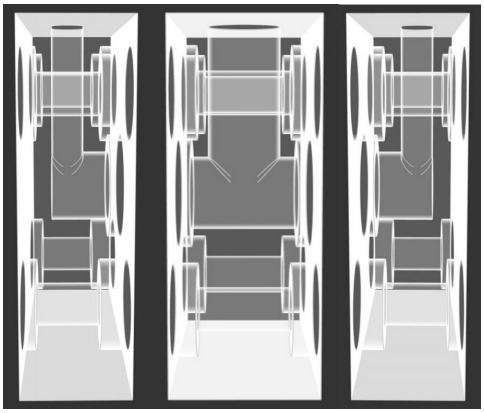

Figure 3.3: Cross section of the assembled cell. From [37].

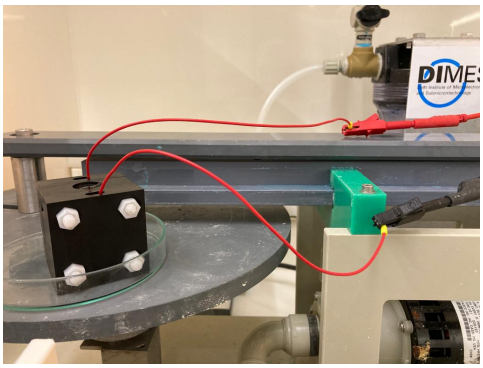

Figure 3.4: The assembled battery connected to the measurement setup.

contact plate is pressed against the electrode by the spring, in a way similar to battery powered everyday appliances such as remote controls and torches. One could also consider pressing the spring directly against the wafer, without a plate in between. However, this plate is used to maximize the contact between the battery and the external circuit. Moreover, without this plate the contact area between spring and wafer is small and hence, the pressure of the spring is concentrated over a small area. This yields a larger chance of the silicon anode breaking. This would cause leakage of electrolyte and disconnecting part of the electrode, halting the discharge. In Figure 3.3 a cross section of the assembled cell is shown. Figure 3.4 shows the cell connected to the measuring equipment.

3.3. Anode

The anode in this work consists of crystalline silicon. As discussed in Section 2.5.3 P-type doped silicon is often preferred over n-type for this application. Theoretically, n-type silicon would yield higher discharge potential, but this is offset by a higher corrosion rate, especially in high concentration electrolyte. In this research both <111> and <100> orientation crystalline p-type silicon wafers have been used. A back contact is applied to the wafer and the wafer is broken up into smaller pieces. This will be discussed in the following two sections.

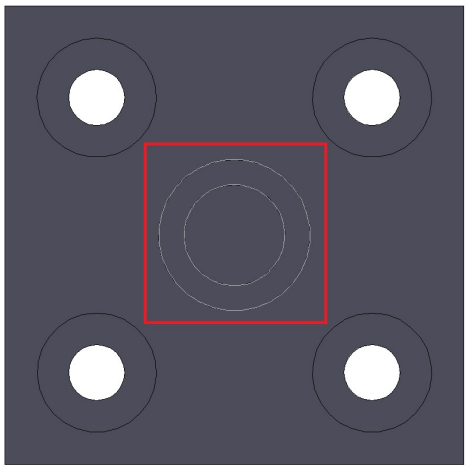

Figure 3.5: The electrolyte-facing side of the side pieces of the used cell in the work by Prins[37]. The perimeter of the anode is indicated in red. As can be seen, the circular hole where the contact sits in the cell is covered by the wafer piece. There is some excess silicon overlapping the edges of the hole. to create a proper seal. A similar setup is used in the work by Durmus et al. [43].

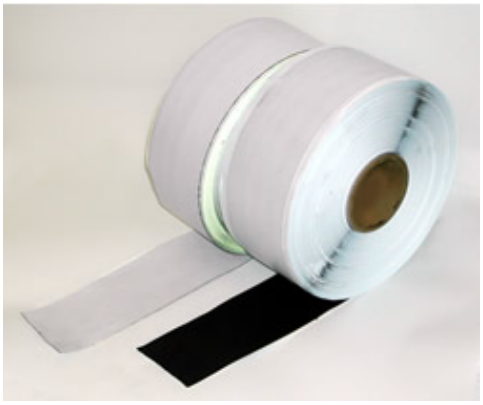

Figure 3.6: Roll of the air electrode produced by ElectricFuel [36]

3.3.1. Current collector

A current collector is used to improve the performance of the battery. Using a Trikon Sigma 204 dealer an aluminium alloy is sputtered on the backside of the silicon wafer. Pure aluminium would potentially yield Al spike forming in the silicon. In microelectronics this alloy is used extensively, and therefore this material is readily available in the Else Kooy Lab. This alloy consists of aluminium and 1% silicon and prevents this spike forming. The Trikon only holds 10-inch wafers, so that is the wafer size of choice.

3.3.2. Laser cutter

Given that the active area in the battery cell is only 1 cm^2, a single wafer can serve as several anodes. Therefore the wafer is split into squares of 2 cm by 2 cm. Using the laser cutter lines are etched in the wafer forming a matrix of squares of 2cm by 2 cm each. After etching, the wafer is easily broken into the individual anodes by hand. The potential defects caused by this process have no influence on the experiments, as they are localized to the lines. The edges of the pieces will be located outside the active area in the battery. Therefore, the lines can be etched on either the front or the back of the wafer.

3.4. Cathode

The air cathode used in these experiments is a commercially available air electrode, produced by ElectricFuel [36]. The goal of this electrode is to keep the electrolyte in the battery, but let oxygen pass through for the discharge reaction. Essentially, it is a membrane. It consists of a nickel mesh, into which activated carbon is pressed. This roll can be cut into pieces using a pair of scissors. In this experiment a piece similar in size to the anode is used.

Prins [37] has shown that it is beneficial to do a pre-treatment of the air electrode before assembling the battery. This is done in the same fluid that is used as electrolyte, the KOH solution. A small amount of the liquid is placed in a container and the piece of electrode that is to be used in the discharge is placed in it. According to Prins' work a pre-treatment of 8 hours is ideal, but a pre-treatment of 4 hours already yields a far better result than no pre-treatment. In this work 6 hours of pre-treatment is used, as this was more convenient for the experiments and the added value of the higher discharge potential as result of the longer pre-wetting was deemed insignificant.

3.5. Electrolyte

The electrolyte in this research is a solution of potassium hydroxide in water. As discussed previously, the concentration of elctrolyte salt has significant influence on the performance of the battery. As discussed in Section 2.3, higher concentration of KOH can support higher discharge potential. On the other hand, higher concentration of electrolyte is also associated to higher corrosion rates. However, the limited conduction of the electrolyte is expected to have larger impact on the overall battery performance. In this experiment a 40% KOH solution is used. This solution is obtained from dissolving KOH pellets in the water. These pellets are assumed to be pure KOH.

3.6. Galvanostatic discharge

The actual performance of the battery is testeted in a galvanostatic discharge experiment. In galvanostatic experiments the current is kept constant and the output potential is evaluated. Currents of $150\mu A$ are evaluated. It is general practice to let the battery stabilize first during a period of no current. To provide the constant current, an Autolab PGSTAT204 is used, combined with the Nova software. The procedure for discharge can be customized in the software.

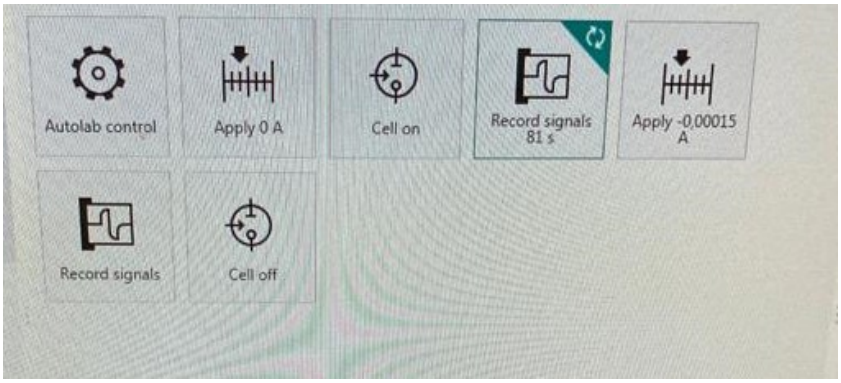

Figure 3.7: A screenshot of the nova software, as used in this work.

Figure 3.7 shows an example of such a procedure. In this example the first block holds the information on the stopconditions and controls for the system. The second block sets a constant current if 0 ampere. There are two blocks that define that the signal is recorded for a set time. The OCP period is also registered. The signal is recorded every second.

3.7. Weight measurement

As described earlier this chapter, the weight difference before and after the discharge is to be recorded. Given that the weight losses are small, a scale is used that can accurately register tenths of milligrams. A weighing balance from All Scales with a resolution of 1 mg and a deviation of 0.1 mg is used in this research.

Figure 3.8: The scale used for the weight measurements

4

Experimental Results

In this chapter the experimental results are discussed. The preliminary goal of the discharge experiments was to reproduce the experimental results obtained by Prins in 2020 [37]. The cell was assembled and connected as discussed in Chapter 3. The anode and cathode were copied from the work of Prins, with the addition that several types of silicon wafers were used. The discharge procedure that was used by Prins in the Nova software was also used in this work. The goal was to obtain discharge potentials and times that were similar for the same parameters, hence the same type of silicon wafer was used, the same electrolyte concentration was prepared and the same discharge recipe with the same current density of 150 µA was selected in the Nova software. In line with the results from Prins the air electrode was pre-wetted for multiple hours. According Prins, 4 hours of prewetting has a noticeable effect. Prewetting for 8 hours would yield the most noticeable increase in discharge performance, but for workflow reasons 4 hours was decided on as EKL had limited opening hours because of the pandemic.

However, it has proven to be hard to reproduce the results reported by Prins, both in terms of discharge potential and discharge time. The results of discharging at 150 µA with an electrolyte concentration of 30% is shown in Figure 4.1. In this experiment first the cell is kept at OCP, after which the battery is discharged at 150 µA. As can be seen, as soon as the current starts to flow the potential drops to 0 in tens of seconds.

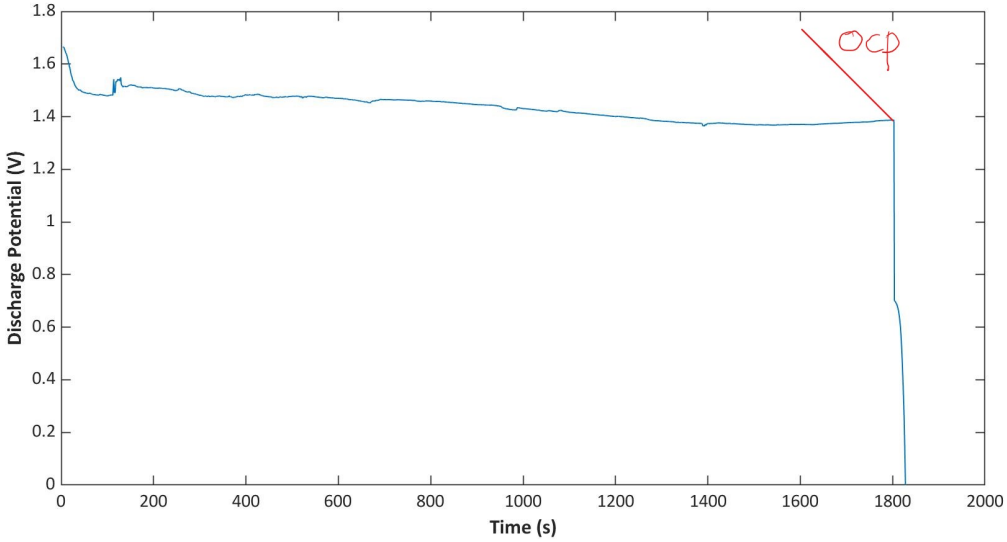

Figure 4.1: Discharge at $150 \mu A$ after 4 hours of pre-wetting

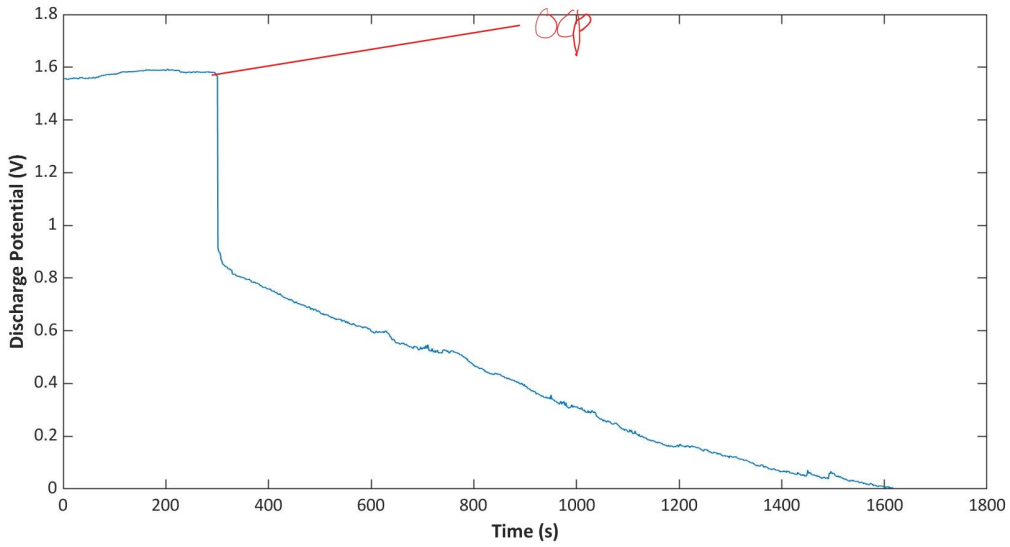

Figure 4.2: Discharge at 8 µA after 4 hours of pe-wetting with 300 seconds of OCP.

In order to overcome this, some alterations to the test were proposed and tested. Firstly, the electrolyte concentration was altered. A range of electrolyte concentrations (here given as weight percentage), spanning from 30% to 60% KOH was used, but this yielded little to no improvement in terms of discharge potential or time. No discharge at 150µA was observed for any of these concentrations.

Next, changes were made to the discharge current density. Many previous research on alkaline silicon-air battery cells, such as the work by Durmus [43] [31] [27] or the work by Park [38], was performed at significantly lower current densities, ranging from as little as 5 µA up to 50µA. This did not yield a significant improvement. In Figure 4.2 the result of discharging at 8 µA is shown. Again, first the cell is kept at OCP for 300 seconds, after which a current of 8 µA is extracted. However, the potential in this cell dropped rapidly to approximately 0.8 V as soon as the current was extracted. Additionally, the potential dropped further over time, and reached 0 V after about 1400 seconds of discharge.

Halfway the experimental stage of this research, the equipment was moved from the MEMS lab to the Cleanroom class 10000. After moving, there was an error in the connection of the system, that caused all discharges after to be unsuccessful. Unrealistically high values for the OCP were recorded, upto 10 volts. After contacting the equipment owner, the setup was examined thoroughly and checked using a simple setup with an AA batteries. This resulted in discharge potentials in the expected range of 1.4-1.5 volts , suggesting that the error was solved. However, this did not yield any successful discharges of silicon-air batteries. The error that was encountered was outside the scope of this research. Therefore the focus of this research shifted towards the simulation of silicon-air batteries in Finite Element Modelling (FEM) software (COMSOL).

In conclusion, in this research no successful discharge can be reported. The reason for this issue remains open for discussion. Several potential solutions were investigated unsuccessfully. Because of this the further experimental research was put on hold and the focus was shifted to FEM simulations.

5

Modeling Methods

In this chapter the approach of the finite element model of a silicon-air battery are described. The model is build to match experimental results from research by Durmus et al. and Prins [27, 31, 37]. The model developed by Prins in 2020 is the starting point of the model presented in this report [37]. In this work COMSOL Multiphysiscs version 5.6 build 401 is used. Comsol is an interactive simulation environment that can be used to model, solve, and simulate a broad range of engineering and science problems. It is designed to be able to implement many different types of physics in a single model [60]. The work by Prins was in turn based on several existing models, published by COMSOL [61–63]. The model is based on the ”Li-air battery” that was published by COMSOL, which was build in the ”Li-ion battery interface” in COMSOL. Many of the parameters discussed in the coming sections are based on or taken from these models. The model is split in three domains: the silicon electrode, the separator (which is filled with the electrolyte) and the air electrode. A schematic representation of this is shown in Figure 5.1.

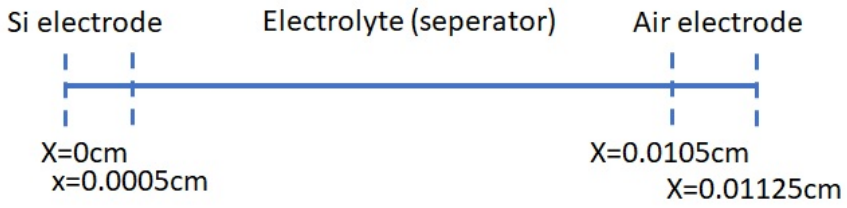

Figure 5.1: Schematic representation of geometry of the siliocn-air cell with the different domains in the 1D-model. This image is not to scale.

Finite Element Modeling, or the Finite Element Method (FEM) is a method for numerically solving differential equations in engineering and many other physical applications. As the name suggests, a structure, in this case a battery, is divided into small or finite elements. These elements are defined by nodes. For each node the applicable system of partial differential equations is solved, including the defined physics for this node.

The three domains are discussed in detail in the coming sections. The relevant electrochemistry as well as the COMSOL inputs and modeling considerations are highlighted.

5.1. Electrolyte and separator

The electrolyte used in this work on alkaline silicon-air batteries is a solution of KOH in deminaralised water. In COMSOL the electrolyte is located in the separator between the electrodes. As discussed in the experimental part of this work in Chapter 3, the electrolyte is produced from KOH pallets. These pallets are dissolved in deminieralised water and the KOH splits into two ions: OH^- and K^+. Potassium

salts dissolve very well in water. This means that all of the KOH splits into the ions and no solid KOH is left, meaning that the electrolyte consists of potassium- and hydroxide ions and water. In Equation 5.1 the dissolution of KOH is shown.

$$KOH \longrightarrow K^+ + OH^- \tag{5.1}$$

COMSOL contains an interface called ”battery with binary electrolyte”(batbe). In a binary electrolyte the two different species exist in a 1:1 ratio. That matches the assumption that the KOH dissolves completely, and therefore this interface is applicable for this model.

5.1.1. Experimental variations in the model

In the experimental work by Prins [37] and Durmus et al. [27, 31, 43] different concentrations of electrolyte are used. To match the experiments by Durmus et al., the initial concentration in the model was chosen to be 5 M, which translates to 5000 $mol \cdot m^{-3}$. The area of the electrodes was 0.44 cm^2. The area in this case is the area of exposed electrode, not the total area of the electrode material that is inserted in the cell, as shown in Figure 3.5. The distance between the two electrodes was 1 cm. These parameters can be easily adjusted for different runs of the model. To match the work by Prins [37] the concentration is increased to 6.91 M, the separator length is increased to 2 cm and the cross sectional area of the electrode is increased to 1 cm^2.

Besides the electrolyte parameters discussed above, there are a number of parameters that are used in the model that are either based on literature or on the experimental setup that is simulated. These are listed in Appendix B. These data mostly consists of empirical values from literature and the previously mentioned example models.

5.2. Silicon electrode

The silicon electrode is the anode of the silicon-air battery. In the experiments by Durmus et al. [27, 31, 43] and Prins [37] monocrystaline silicon wafers of different doping levels are used. As described in Chapter 2, besides the anodic half-cell reaction, two other reactions take place at the anode: corrosion and passivation.

In the lithium-air battery model that is included in the COMSOL software the anode is modeled as a boundary, with boundary conditions to represent the lithium. For the silicon-air model this is insufficient. The deposition and dissolution of reaction products at the anode is of significant importance for the functionality of a silicon-air battery. Therefore, Prins [37] modelled the silicon anode as a porous electrode, similar to the cathode, with depositing and dissolving species. In the model of Prins [37] the discharge is modelled such that all the silicon that is used in the discharge is deposited as silicon oxide on the silicon anode directly. The reaction as modelled by Prins is:.

$$Si + OH^- \longrightarrow SiO_2 + 4\,e^- \tag{5.2}$$

Furthermore, the silicon was assumed to be infinite and corrosion was not included in the model in order to investigate other parts of the battery.

A closer representation of reality would be a model where the discharge and passivation reaction are split in two distinct reactions, with the inclusion of corrosion. In the coming section the different reactions, the metal-semiconductor interface and the parameters of the anode are described.

5.2.1. Discharge half-cell reaction

As discussed in Section 2.3, during discharge the silicon in the wafer reacts with the electrolyte under formation of silicic acid, $Si(OH)_4$, releasing 4 electrons. This reaction is:

$$Si + 4\,(OH^-) \longrightarrow Si(OH)_4 + 4\,e^- \tag{5.3}$$

The equilibrium potential of this reaction is -1.69 V [30]. The silicic acid can dissolve in the electrolyte to some extent. When the maximum amount of silicic acid is dissolved in the electrolyte, or when the rate of dissolution becomes insuficient, the passivation reaction that will start.

Reaction 5.3 is modelled in the COMSOL software in the porous electrode node. The discharge reaction is defined in the electrode reaction. The local current density in the electrode is described by the Butler-Volmer equation [64]:

$$j_{loc} = j_0 \left[C_r \exp\left(\frac{\alpha_a F \eta}{RT}\right) - C_o \exp\left(\frac{-\alpha_c F \eta}{RT}\right) \right] \tag{5.4}$$

Where:

$$\eta = E - E_{equilibrium} \tag{5.5}$$

This equation forms the basis for the electrode potential in COMSOL.«
In this equation j_{loc} is the local current density and j_0 is the exchange current density, both in A·m^{-2}. The anodic and cathodic transfer coefficients are given by α_a and α_c. Both are dimensionless. F is the faradaic constant in C·mol^{-1}, R is the general gas constant in J·(mol·K)$^{-1}$ and T is the temperature in K. The overpotential η is the difference between the actual potential E and the equilibium potential $E_{equilibrium}$. Last, C_r and C_o are dimensionless coefficients based on the concentrations of reduction and oxidation reactants and products.

5.2.2. Passivation

When more silicic acid is produced than can be dissolved in the electrolyte, the passivation reaction starts. In this reaction no charge is transferred to or from the reactants. No electrons are absorbed or released. The formation of SiO_2 is given by:

$$Si(OH)_4 \longrightarrow SiO_2 + 2\,H_2O \tag{5.6}$$

As discussed in Section 2.4 the formed oxide is in fact some form of a suboxide of changing composition. This is simplified to single conductivity for the full discharge, even though the conductivity of the oxide changes as the silicon is more fully oxidized. The fully oxidized oxygen (SiO_2) is far less than the conductivity of the initial suboxide.

Because of the absence of charge transfer, the reaction is modelled as a so called non-faradaic reaction. A non faradaic reaction is a reaction that is not electrochemical in nature, and hence there is no charge transfer. Non-faradaic reactions are used in COMSOL to define reactions for dissolving and depositing species at the boundary between the electrolyte and anode. The reaction rate of this reaction can be defined individually.

As the passivation takes place, the passivating silicon oxide layer is formed on the electrode surface. Mathematically this is modelled in COMSOL according to:

$$R_{film} = \frac{s_0 + \Delta S}{\sigma_{film}} \tag{5.7}$$

In this equation R_{film} is the resistance over the film in Ω. s_0 is the initial thickness of the film in m, which is set to zero. ΔS is the increase in thickness of the layer over time. This depends on the deposition rate. The conductivity of the material is denoted by σ_{film}, given in S·m^{-1}. This is set to 6.7×10^{-4} S·cm^{-1} [41]. These values are converted to end up matching the output in Ω.

5.2.3. Corrosion

The corrosion mechanism as discussed in Section 2.5 is a complex system of several chemical reaction steps. In the reaction there is no net charge transferred in or out the silicon electrode. Furthermore, the model as it is presented in this thesis is a 1D model, which means that anodic and cathodic sites are not defined, as these would be located on a plane at the same 1 dimensional position, orthogonal to the direction in which the model is defined. Therefore, this can be defined as a chance that places

are eather anodic or cathodic sites. Because of this, the corrosion reaction is simplified to a non-faradaic reaction, where no charge is transferred, similar to how the passivation reaction is modelled. This means that the overall effect of the corrosion can be observed (i.e. the additional consumption of silicon), but not the more detailed effect of electron concentration on the corrosion rate.

This means that the modelled reaction is the overall corrosion reaction, shown in Equation 5.8 disregarding the anodic and cathodic sites:

$$Si + OH^- + 2\,H_2O \longrightarrow SiO_2(OH)_2^{2-} + 2\,H_2 \tag{5.8}$$

Effectively this means an additional source of silicon dissolution in the model, in addition to the anodic half-reaction.

In COMSOL the H_2O concentration is not considered and the formed hydrogen gas is neglected, as it will go out of solution quickly. However, this means the potential hydrogen gas bubble formation at the anode is disregarded. This is justified as it is generally indicated in literature to be insignificant [43][32]. Because of the way the non-faradaic reaction is modelled, the corrosion rate is a variable in itself, rather than being linked directly in the model to other model parameters such as potential, current density or electrolyte concentration. This allows for the adjustment of this parameter in itself, but at the cost that it disregards many of the intricate effects of corrosion in silicon-air batteries, most notably the electron concentration.

5.2.4. Metal-semiconductor contact

As discussed in Section 2.7, a contact between metals and semiconductors will often result in a so called Schottky barrier. This implies that part of the potential is lost in this contact. In the model presented in this paper this potential drop is modelled in a simplified way. In practice, the potential drop is dependent on the forward or backward bias, or current. In this model the Schottky barrier is modelled as a given drop in potential. The value of this drop is strongly dependent on the materials that are used. In the work by Durmus et al. [31] a highly As doped silicon wafer (resistivity of 0.001Ω-0.007Ω) is used. This quite low resistivity means that the doping concentration is between 7×10^{18} cm^{-3} and 1×10^{20} cm^{-3}. From Equation 2.9 follows that the gap between the conduction band and the Fermi level is quite small. The electron affinity of silicon is about 4.01 [56] and from Equation 2.11 it follows that the work function of the silicon is about 4.04 eV.

In the work by Durmus et al. [43], the wafer is pressed against a stainless steel contact. The work function of stainless steel is about 4.4 eV [65]. This means that the Schottky barrier has a height of about 0.36 eV.

5.2.5. Porosity and specific surface area

The silicon anode is modelled as a porous electrode. This implies that the porosity needs to be defined for the electrode. From previous research by Park et al., Sarwar et al. and Zhong et al. [32, 38, 66] the porosity of the silicon wafer has a tremendous effect on the overall performance of the battery. Even though in these works different methods were used to achieve this, effectively their processes yielded a textured silicon surface resulting in an increased surface area. In short, a higher porosity will yield a larger surface area on the surface of the silicon. First, this means that there is more surface area for the electrolyte to contact the silicon wafer where the discharge reaction can take place. Second, this means the surface where the passivating oxide layer can deposit is larger, leaving a larger surface unpassivated.

A parameter that is linked to the porosity is the specific surface area. The specific surface area is a measure for the exposed surface area per unit volume, in $m^2 \cdot m^{-3}$ [67]. To elaborate: two samples with identical values for the porosity can have completely different specific surface areas, dependent on the particle size and pore size. When considering densely stacked spheres, a sample with large particles will have a relatively low specific surface area, whereas a sample with small particles will have a relatively high specific surface area. In this model nano-textured silicon is considered, which means small particle size and small pore size, resulting in high specific surface area relative to the pore size.

5.3. Air electrode

In the silicon-air battery an air electrode is used as cathode. In the COMSOL software an example model of the lithium-air battery is available [61]. In this model the functionality of the air electrode is very similar to that of the air electrode in a silicon-air battery. Therefore, the air electrode is modelled in a similar way. Because of this, many of the parameter values in the model are also taken from the lithium-air model.

5.3.1. Electrode reactions

The air electrode has an equilibrium potential of 0.40 V [32], the standard electrode potential of the half-cell reaction of oxygen with water. This reaction is described in more detail in Section 2.3, and repeated below:

$$O_2 + 2\,H_2O + 4\,e^- \longrightarrow 4\,OH^- \tag{5.9}$$

The electrochemical dynamics of the air electrode are best described by the Butler-Volmer equation, shown in Equation 5.4.

5.3.2. Oxygen in the electrode

As oxygen diffuses from ambient air into the battery, the air electrode is a membrane through which this oxygen diffuses. The electrode is modelled as such. The same as in the lithium-air battery [61] the air electrode is modelled as a porous electrode with high porosity. The porosity was set to 73%, which means there was 27% of solid material. In the model the pores are completely filled with electrolyte.

The transport of the dissolved oxygen in the electrolyte through the porous electrode is modelled in COMSOL using the ”transport of diluted species(tds)” interface. This interface models the concentration of oxygen in the electrolyte throughout the electrode. The oxygen concentration outside the battery is set to the oxygen concentration of atmospheric air at atmospheric pressure. The oxygen concentration at the boundary between ambient air and the electrode is calculated as the product of the atmospheric oxygen concentration and a solubility factor. In the lithium-air battery model by COMSOL [61] this solubility factor is set to 0.4. In the work by Prins [37] it was shown that this solubility factor has a significant impact on the discharge potential, varying between 0.9 V for a solubility factor of 0.2 and 1.4 V for a solubility factor of 0.8 at a discharge current of 150 µA. This can be expected, as the solubillity factor influences the dissolution rate, which in turn influences the oxygen concentration in the electrode. H_2O is readily available at the electrode/electrolyte boundary, so the oxygen concentration is rate limiting in the reaction shown in Equation 5.9.

5.4. Time-dependent solver and parametric sweep.

As discussed in the introduction to this chapter, finite element models rely on differential equations that are solved on given positions in the defined model. These points form the so-called mesh. In the case of this model this means that the domain is split into 44 separate computational domains and for each of these domains a system of coupled partial differential equations is solved using a time-dependent solver. A time-step is defined in the model, the size of which depends on the desired resolution of the results. In the case of this model a time-step of 10 seconds sufficient to identify the trends in the results. To increase the resolution a finer time-step can be defined in COMSOL, but this will result in larger computational cost and longer computational time. To save computational power, also a courser time-step can be defined for iterations of the model that simulate longer periods, but this is obviously at the cost of resolution.

To identify the effect of the parameters in the model, a parametric sweep is used. A range of values can be set for any given parameter in the model. This parameter is then varied between the set values and for each of these results are modelled. In this way the effect of a single parameter on the results can be clearly shown.

6

Modeling results

The results that are produced from the model discussed in the previous chapter are highlighted in this chapter. To be able to draw any conclusions from these results, it is important that these results can be compared to experimental data. As discussed in Section 5.1.1 some of the parameters can be easily adjusted to match the simulated experiment. Several effects have been studied in literature and the results produced by the model for these experiments are compared to the experimental results as published. The results are compared to work by Durmus et al. [27, 31, 43], Prins [37], Sarwar et al. [66], and Zhong et al. [32]. Furthermore, the effects of the added complexities in the model are discussed, especially the effects of corrosion and passivation. Unless specified otherwise, the generated model outputs are for 86400 seconds (24 hours). This is because most experimental data that are used as comparison are published for the same duration of discharge.

In Figure 6.1 the discharge mechanism is schematically represented, including the passivation and corrosion. In this illustration part of the electrons in the discharge reaction will move to cathodic sites where these will take part in the cathodic sites reaction of the corrosion mechanism. This means that a fraction k of the electrons produced in the discharge reaction is not used in the external circuit, and hence, part of the silicon is consumed in the corrosion rather than in the discharge. Because the corrosion is modelled as a non-Faradaic reaction, without considering the half-reactions where the electrons are transferred, the corrosion is modelled without concerning these electrons. The formed $Si(OH)_4$) is dissolved in the electrolyte and can either stay in the electrolyte, where it can further react to form its conjugate base $Si(OH)_2^{2-}$, or it takes part in the passivisation mechanism.

This chapter starts of from the model published by Prins [37]. In the first section the results with the passivation reaction as discussed in Section 5.2.2 are discussed. Then the next layer of complexity is added with the inclusion of the corrosion mechanism. Third, the specific surface area is discussed as an influential parameter for the model. Fourth, the results of the inclusion of the back-contact as described in Section 5.2.4 are discussed. Note that for the three preceding parts the metal back-contact is already included in the shown results, as its influence on parameters besides the observed discharge potential is limited. Last, the results from the model are compared to two experiments for validation: the discharge potential for different discharge currents and the discharge potential for different electrolyte concentrations.

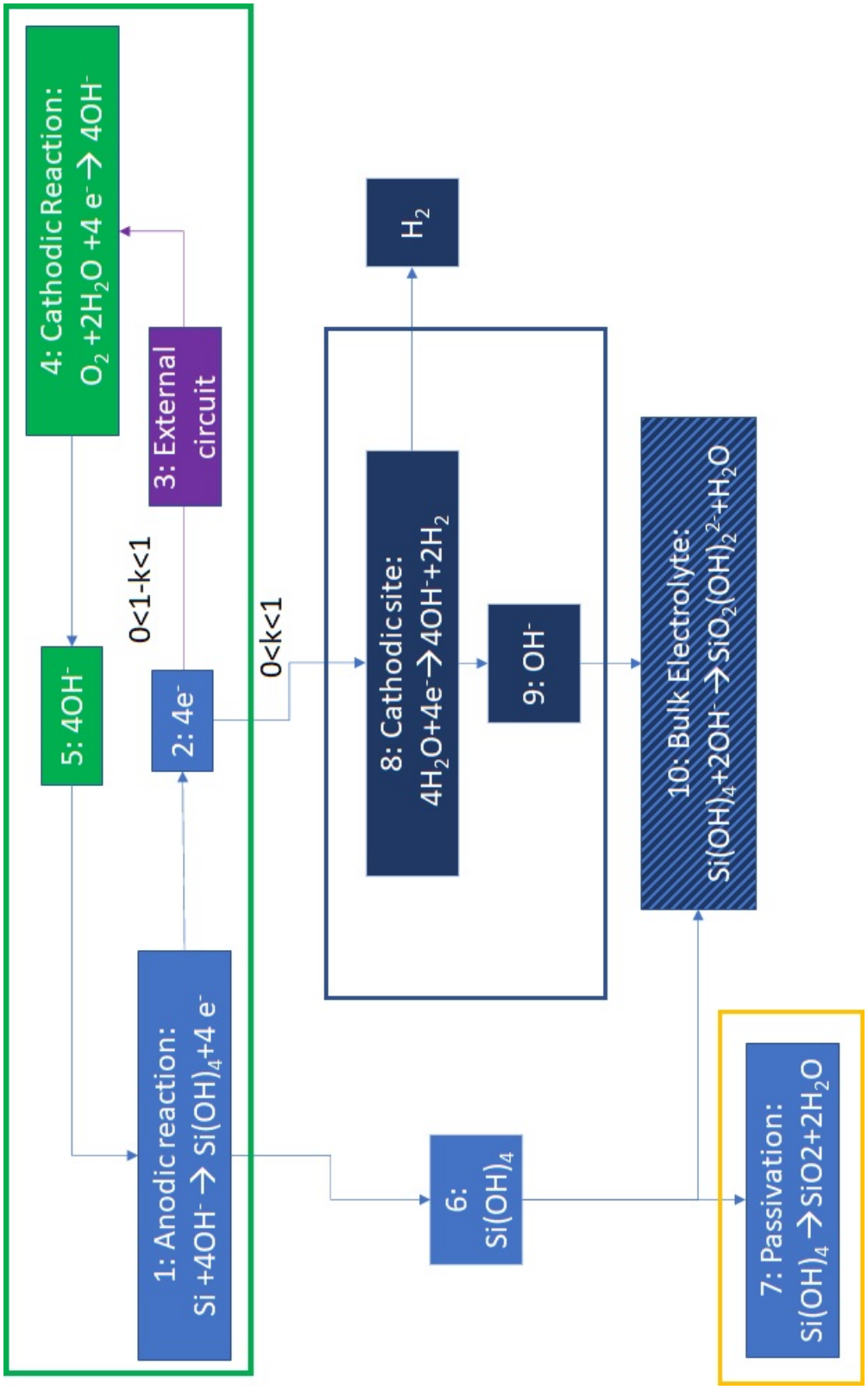

Figure 6.1: In the block diagram the discharge-, corrosion- and passivation mechanisms are illustrated. The discharge mechanism is encircled by the green box, where the green reactions are on the cathode, and the blue reactions are at the silicon anode. The fraction k represents the fraction of the electrons, and therefore indirectly the faction of the silicon, that is consumed in the corrosion mechanism. The passivation half-reaction at the cathodic sites is encircled by the dark blue box. The passivation reaction is encircled in yellow.

6.1. Passivation reaction

In the original model by Prins [37] all silicon consumed in the discharge process was deposited as silicon oxide directly. In the model presented in this work the silicon is first dissolved into the electrolyte, after which the passivation is modelled as a secondary reaction. Instead of using a film resistance at the silicon-electrolyte interface, a growing film on the surface of the electrode is modelled. The discharge current and battery cell dimensions were adjusted to match the discharge current in the work by Durmus et al. [31] so that the results later on in this chapter can be compared to their work.

The passivation reaction is in fact the formation of an insulating layer on the surface of the silicon electrode. The deposition rate is dependent on the concentration of constituents in Reaction Equation 5.3 and the reaction kinetics. But more importantly, the conductivity of the formed layer has a significant effect on the discharge. The potential drop over the film increases for decreasing conductivity. The range of conductivities is between the conductivity of SiO_x of 6.7×10^{-2} $S\cdot m^{-1}$ as reported by Kim et al. [41] and the conductivity of fully oxidized silicon (SiO_2) as reported by Gauthier [42] in the order of 10^{-10} $S\cdot m^{-1}$.

The results shown in Figure 6.2 clearly show that the discharge of the silicon air battery is influenced significantly by the film condctivity of the deposited oxide layer. For a conductivity of 1×10^{-10} $S\cdot m^{-1}$ the discharge was halted after only a few minutes. Increasing the conductiviy to 1×10^{-8} $S\cdot m^{-1}$ yields a discharge of over 15 hours. For the conductivity of the suboxide as reported by Kim et al. [41] of 0.067 $S\cdot m^{-1}$ the discharge potential is more or less constant over the simulated period of 24 hours. The same holds for the 1×10^{-4} $S\cdot m^{-1}$ conductivity. These two plots overlap. For a conductivity of 1×10^{-6} $S\cdot m^{-1}$ the potential is still quite stable and only drops slightly towards 24 hours.

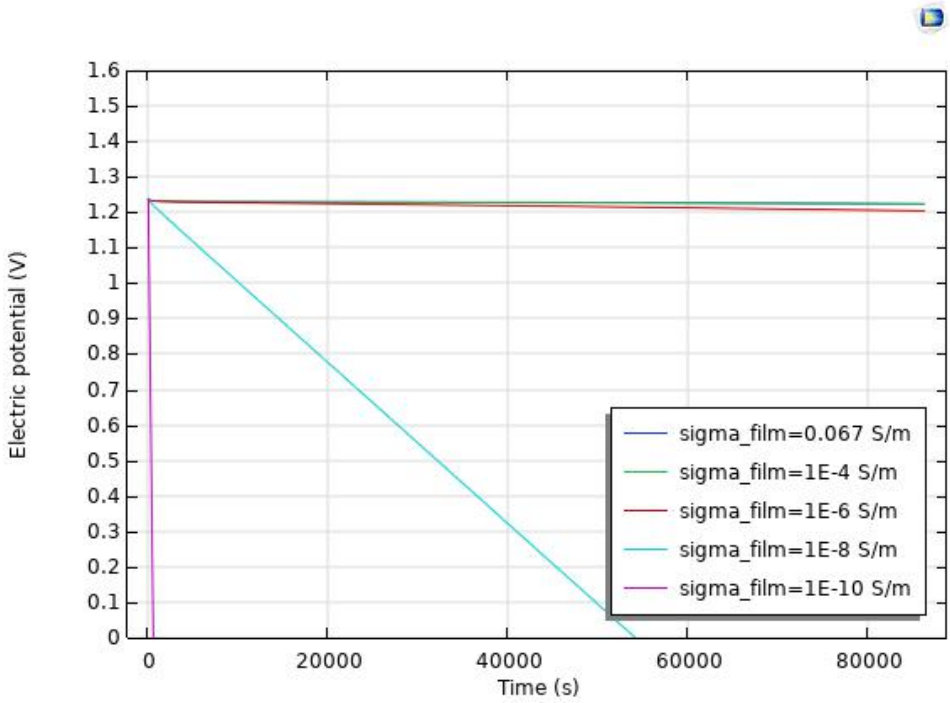

Figure 6.2: This graph shows the discharge potential over time for different conductivities of the oxide layer that is formed on the surface of the electrode. The discharge potential decreases significantly quicker for a lower conductivity. Note that the graphs for the two highest conductivities are nearly identical on this range. The discharge current for this figure is 0.5 $A\cdot m^{-2}$, or 50 $\mu A\cdot cm^{-2}$

6.2. Corrosion

With the introduction of the corrosion reaction into the model, one would expect that more silicon is consumed. However, because of how the model is build, the amount of consumed silicon cannot be easily plotted. This can only be shown indirectly by means of the concentration of silicon products in the electrolyte near the surface of the electrode. In this case the concentration of silicon products in the electrolyte is simplified so that it is only $Si(OH)_4$ and not its conjugate base, as the corrosion is modelled as a non-Faradaic reaction and therefore these would be viewed as the same compound for this reaction. One can expect limited to no effect of the corrosion reaction on the discharge potential, as the half cell potentials of the half-reactions of the discharge mechanism are not influenced by the corrosion mechanism.

In Figure 6.3 the concentration of $Si(OH)_4$ is plotted for when the corrosion reaction is turned on ($a = 1$) and for when the corrosion is turned off ($a = 0$). The binary parameter a is introduced in the model so that the corrosion can be turned on and off in a parametric sweep.

From literature it is known that the corrosion reaction will consume a significant fraction of the silicon compared to the silicon consumed in the discharge reaction. According to Durmus et al. [31] and Zhong et al. [32] one can expect about 90% of the silicon to be consumed in the corrosion reaction. In Figure 6.3 after 24 hours the concentration is about 750 mol·m^{-3} when the corrosion mechanism is turned on, the green line, and about 50 mol·m^{-3} when the corrosion mechanism is turned off, the blue line. This means that without corrosion only approximately 6.7% of the silicon is consumed compared to the case with corrosion. This indicates that a significant portion of the silicon is consumed in the corrosion rather than in the discharge.

In Figure 6.4 the discharge potential for the above mentioned two cases is shown. As expected, the effect of the corrosion on the discharge potential is limited.

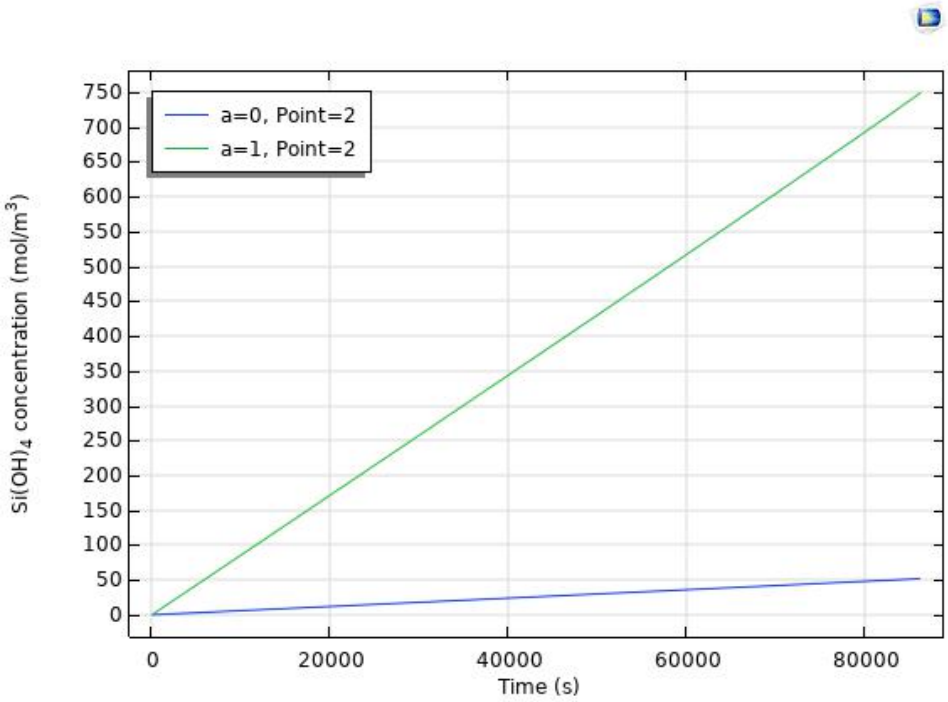

Figure 6.3: In this figure the concentration of $Si(OH)_4$ is shown for a discharge without corrosion in blue. The concentration for discharge with corrosion is shown in green. The discharge current is set to 0.1 A·m^{-2}. For the discharge with corrosion the concentration is 750 mol·m^{-3} after 24 hours. For the discharge without corrosion this number is 50 mol·m^{-3}.

To put this concentration into context, the expected concentration for the case without corrosion can be easily calculated. Current I is defined as charge q over time t, so the unit of amperes is Coulombs

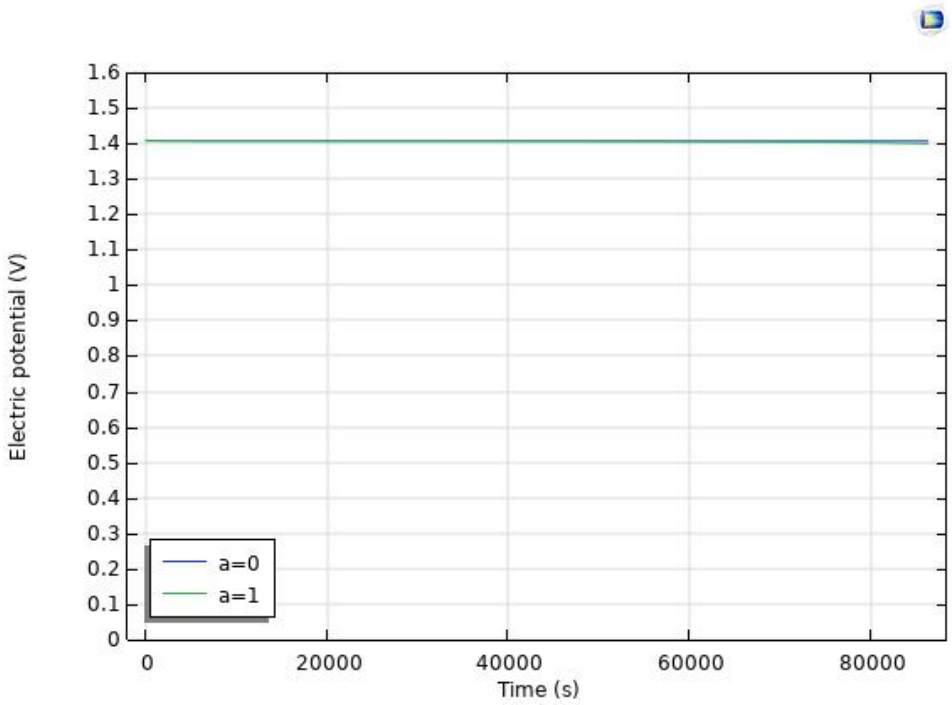

Figure 6.4: In this figure the discharge potential as a function of time is shown for a discharge without corrosion in blue. The discharge with corrosion is shown in green. The discharge current is set to 0.1 A·m^{-2}. It is clear that there is no significant difference between the two discharge potentials and they overlap mostly.

over seconds. Therefore the transferred charge can be calculated using:

$$q = I \cdot t = 50\mu\text{A} \cdot 86400\text{s} = 4.3\text{C} \tag{6.1}$$

The amount of electrons n in moles is:

$$n = \frac{q}{F} = \frac{4.3}{F} = 4.5 \times 10^{-5}\text{mol} \tag{6.2}$$

F is the Faraday constant in C·mol^{-1}. Given the 4 electrons in the discharge reaction, this means that the consumed silicon is about 1.1×10^{-5} mol. The electolyte volume is 1 cm^3. Therefore the overall expected concentration of silicon in the electrolyte would be 11 mol·m^{-3}, which is the same order of magnitude as the shown results. The results are plotted for a position near the interface between the electrode and electrolyte. When the reaction product is not homogeneously distributed in the electrolyte, this can lead to a higher concentration of the reaction product near the electrode. This is an explanation for the higher concentration found in the model.

6.3. Specific surface area

An important parameter in the model is the specific surface area. This is defined as the surface area per unit volume, in $m^2 \cdot m^{-3}$. The importance of this parameter was already shown in the model by Prins [37]. In the model as presented, this parameter was found to be of significant influence on the discharge potential, especially for higher discharge current densities.

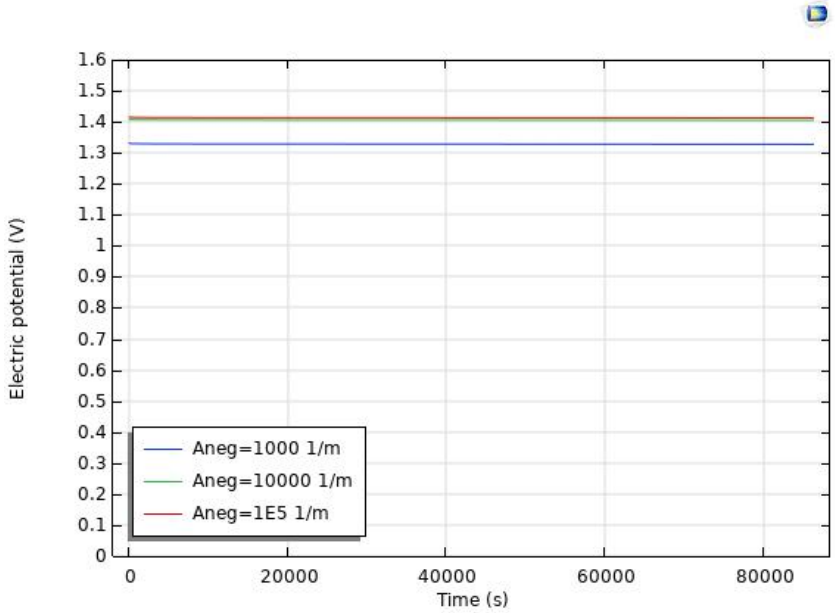

Figure 6.5: The discharge potential as a function of time for a discharge curent density of 0.1 $A \cdot m^{-2}$ increases with an increasing specific surface area. The parameter for specific surface area is called *Aneg* in the software.

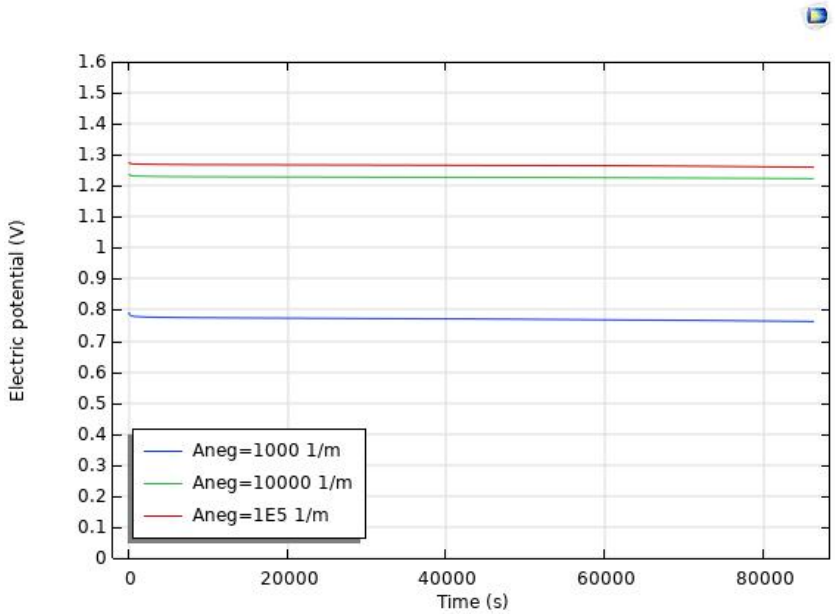

Figure 6.6: The discharge potential as a function of time for a discharge potential of 0.5 $A \cdot m^{-2}$ increases with an increasing specific surface area. The parameter for specific surface area is called *Aneg* in the software.

Figure 6.5 shows the discharge potential at 0.1 $A \cdot m^{-2}$ for different specific surface areas and Figure 6.6 shows the discharge potential at 0.5 $A \cdot m^{-2}$ for different specific surface areas. Comparing these plots, it can be concluded that the drop in discharge potential as the current increases is more pronounced

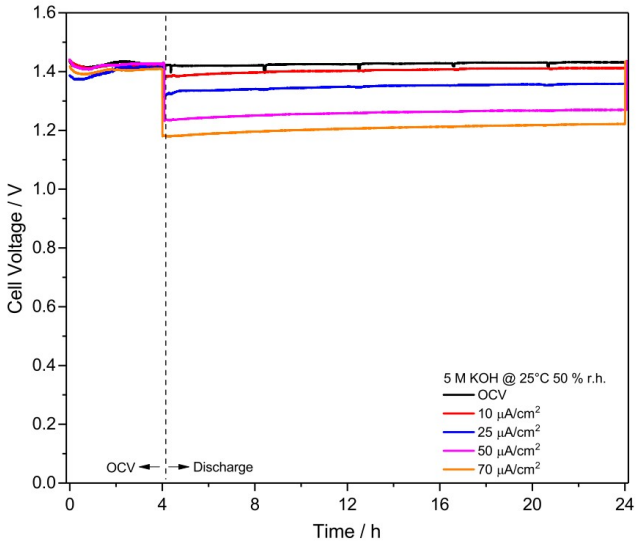

Figure 6.7: This figure shows experimental values of electrical discharge potential as a function of time for a number of discharge currents. These data were obtained from experimental work by Durmus et al. [31]. The electrolyte concentration was 5 M. It is clear that a higher discharge current yields a lower discharge potential.

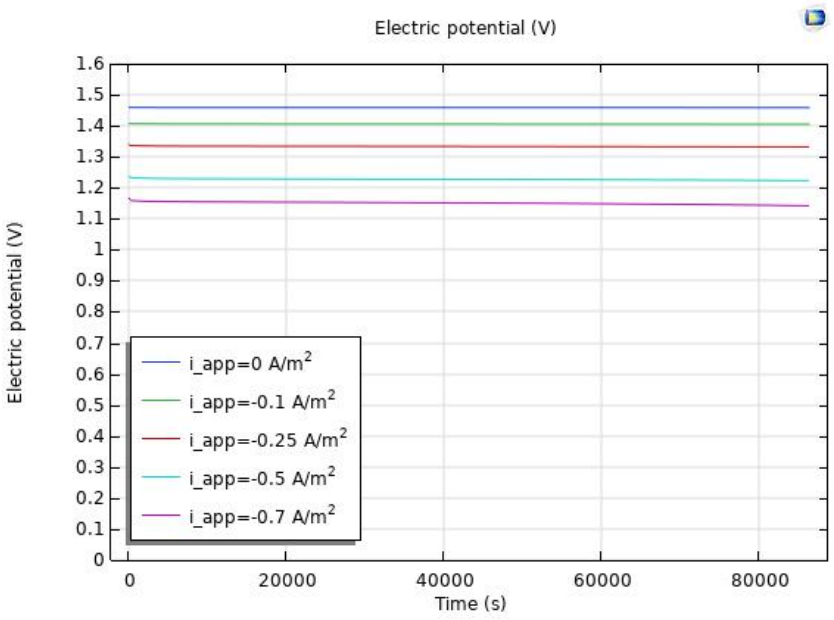

Figure 6.8: The discharge potential over time decreases for lower discharge currents.

for smaller specific surface areas. This can be explained by the smaller interface between electrolyte and electrode, leading to a more pronounced effect of the passivation reaction and less dissolution of reaction product into the electrolyte. In the work by Durmus et al. [31], shown in Figure 6.7 the effect of an increase in current is notable, but not as pronounced as for the smallest specific surface area plotted in Figure 6.5 and Figure 6.6. To match the simulation results to the experimental results, the specific surface area is set to 10^5 $m^2 \cdot m^{-3}$. As can be seen from Figure 6.8 the difference in discharge potential is for the different discharge current densities is similar to the reported values in Figure 6.7.

6.4. Backcontact

To simulate the metal back contact on the anode, a voltage drop is added at the back of the silicon. One would expect that this yields an overall drop of the voltage. The magnitude of this drop depends on the height of the Schottky barrier. The open-circuit potentials for different metal-semiconductor contacts is shown in Figure 6.9.

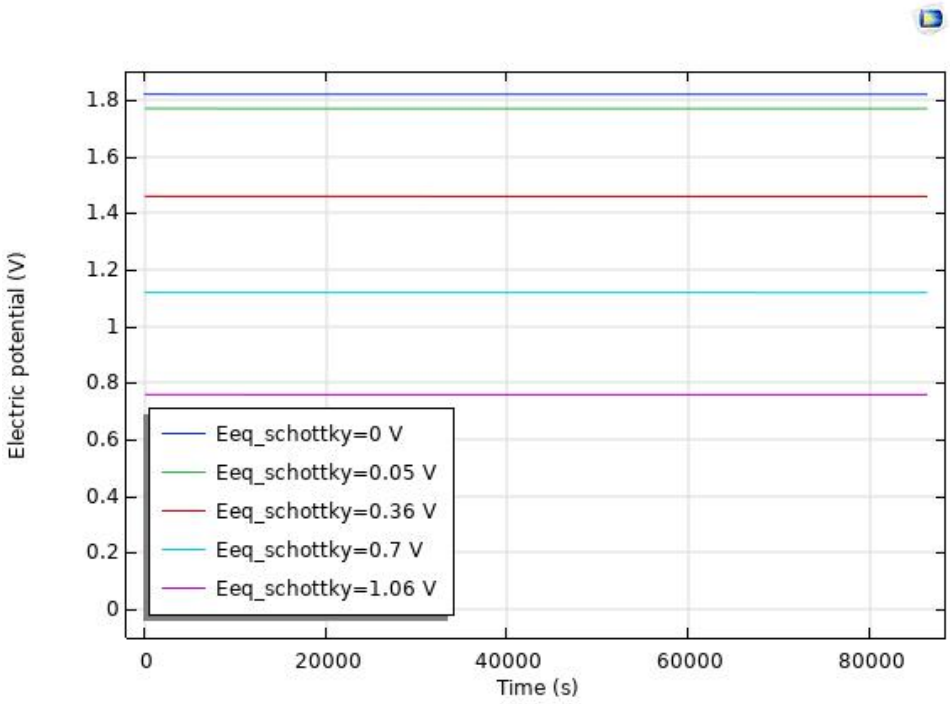

Figure 6.9: The open-circuit voltage as a function of time for different metals. The metals form a back contact on the n-type silicon from the work by Durmus et al. [31], discussed in Section 5.2.4. This is compared to a 0 V drop, which represents no Schottky barrier. 0.05 V corresponds to aluminium, 0.36 V corresponds to a stainless steel back contact, 0.7 V corresponds copper and 1.06 corresponds to gold [65]. Note that in this figure the vertical axis is between 0 V and 1.9 V to show all the plots, whereas the vertical axis in 6.7 is between 0 V and 1.6 V.

These results can be compared to the open-circuit potential in the work by Durmus et al. [31]. From correspondence with dr. Durmus himself it was known that in the experimental work by Durmus et al. the silicon anode was pressed against a stainless steel contact. With the given highly doped n-type silicon that would correspond to a Schottky barrier height of 0.36 V, the light blue line in Figure 6.9. The open-circuit voltage in this instance is 1.45 V.

In Figure 6.7 the open circuit voltage (the curve plotted in black) is approximately 1.42 V. This is similar to the simulated discharge potential for a Schottky barrier of 0.36 V presented in Figure 6.9.

6.5. Discharge current

In Figure 6.7 the discharge potentials for different discharge currents are shown, as reported by Durmus et al. [31]. In Figure 6.8 the effect of discharge current on the discharge potential in the COMSOL model is presented. These two plots are combined in Figure 6.10.

As the discharge current increases, the discharge potential decreases. This was also observed in Figure 6.7. As discussed in Section 6.3, the spread between discharge currents was matched to Figure 6.7 by changing the specific surface area. With the chosen value for the specific surface area (called ”Aneg” in the model) the simulation results are quite similar. This means that the effect of the discharge current on the discharge potential in COMSOL is about 0.1 V off for the highest current density and for the open circuit voltage. The results for 10 µA·cm^{-2}, 25 µA·cm^{-2} and 50 µA·cm^{-2} are more or less aligned.

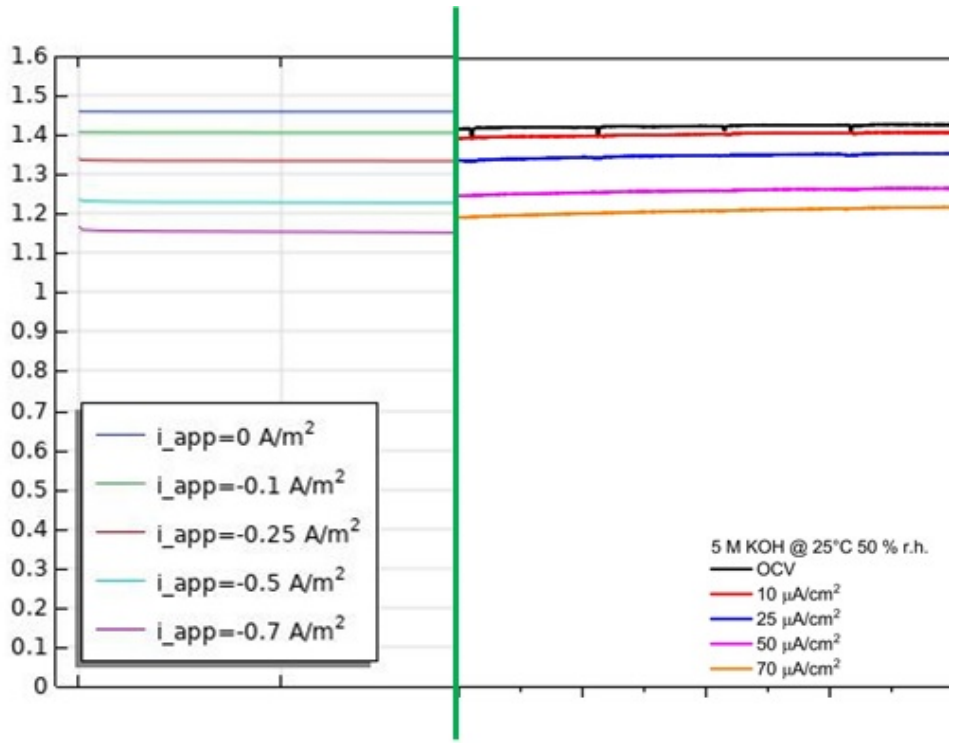

Figure 6.10: Here Figure 6.7 and Figure 6.8 are shown combined. Left of the green vertical line are the data from Durmus et al. [31], and right of the green line are the simulated results.

6.6. Electrolyte concentration

One of the parameters that is often varied in experimental work is the concentration of the electrolyte. This variable can be used to compare the COMSOL model to experimental work, and test the accuracy of the model. In the work by Durmus et al. [31] a higher concentrations of the electrolyte led to somewhat higher discharge potentials.

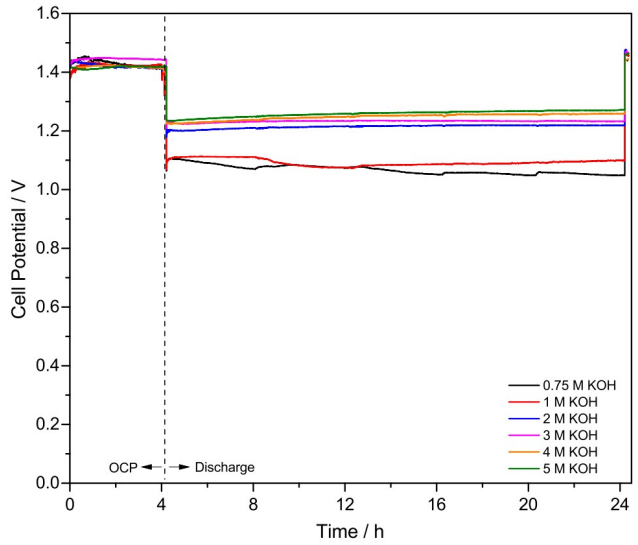

Figure 6.11: This figure shows experimental values of electrical discharge potential as a function of time for a number of electrolyte concentrations. These data were obtained from experimental work by Durmus et al. [31]. The discharge current is set to 0.5 $A \cdot m^{-2}$, or 50 $\mu A \cdot cm^{-2}$. It is clear that a higher concentration of the electrolyte yields a higher discharge potential.

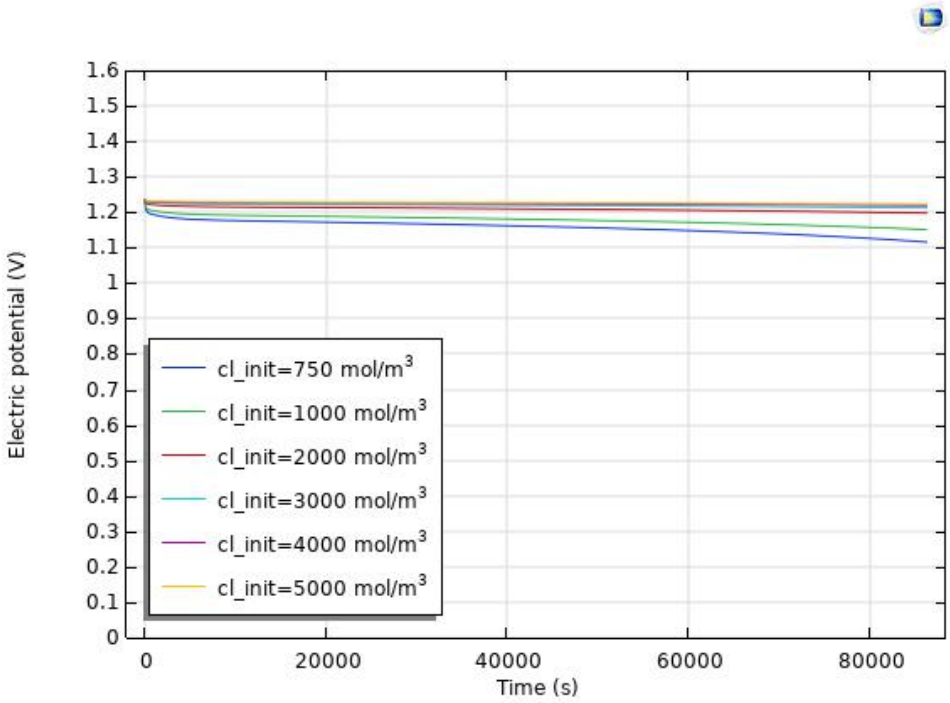

Figure 6.12: The simulated discharge potential as a function of time for different electrolyte concentrations. The discharge current was set to 0.5 A. In this figure, higher concentrations of the electrolyte show higher discharge potentials. The different electrolyte concentrations were set to match the concentrations in the work by Durmus et al. [31] shown in Figure 6.11.

In Figures 6.11 and 6.12 similar trends can be observed: for higher electrolyte concentrations higher discharge potentials can be observed. Especially for electrolyte concentrations between 2 M and 5 M the simulated discharge potentials seem to line up quite well with the experimental data. However, the electrolyte concentrations below 2 M in Figure 6.11 seem to have a relatively low discharge potential. This effect is not seen in the simulated plot.

7

Discussion

In this thesis a finite element model for an alkaline silicon-air battery is developed. A previously existing model formed the basis of this work. Several processes regarding silicon-air batteries have been added to this model. First, the passivation reaction was further developed compared to the original model by Prins [37]. Second, the corrosion reaction was introduced in the model. Furthermore, a metal-semiconductor contact was added to simulate a metal contact on the silicon anode. All these processes combined make for a more complete model of an alkaline silicon-air battery. The results presented in the previous chapter are quite similar to the behaviour that has been published in earlier experimental work by Cohn et al. [29, 30], Durmus et al. [27, 31, 43], Park et al. [38], Prins [37], Sarwar et al. [66], and Zhong et al. [32].

The passivation of the silicon electrode is modelled in a two-step process, that is a closer representation of reality than the original model where all the reaction products were directly deposited on the electrode surface. In the new approach the discharge products are dissolved in the electrolyte, after which in a second reaction they can deposit on the silicon anode and form the passivating oxide layer. In the passivation of the silicon electrode the parameters of the deposited oxide layer have been shown to impact both the discharge time and discharge potential. For higher conductivity of the oxide layer, the passivating properties of the oxide layer are less pronounced, as the potential drop over this layer is smaller. For a low conductivity of the deposited film the discharge was halted after only a few minutes, whereas a higher conductivity produced a discharge of over 24 hours. If the access to the unconsumed silicon was limiting in this model, the conductivity of the layer would have little to no influence on the passivation process. However, it was shown that this conductivity does in fact have a tremendous effect on the discharge time , and therefore it appears that the access to silicon is not the limiting factor in this case. An explanation might be that the model is build in 1D. Therefore the effect at the silicon-electrolyte interface can be described as the average effect over the whole surface of the electrode. One can expect that when the passivating layer is formed, this will not be at the same rate all over the elctrode. A closer representation of reality would be if the localized buildup of this passivating layer on the electrode was included in the model.

Furthermore, the specific surface area was shown to have significant impact on the discharge potential, especially for higher discharge currents. A higher specific surface area leads to a larger contact area between the silicon and the electrolyte. Therefore, the dissolution rate of the reaction product from the discharge reaction into the electrolyte is higher, leading to a longer discharge and higher discharge potential, as the passivation reaction is delayed. Additionally, the increased surface area means that a larger area needs to be covered before the whole electrode is passivated. This is in line with the work by Park et al. [38], Sarwar et al. [66], and Zhong et al. [32]. All these publications have utilised some etching technique to create nano-porous silicon that lead to an extended discharge of the battery, at higher discharge potential.

The corrosion reaction is known to consume a significant part of the silicon. Durmus et al. [31] have reported that about 97% of the silicon mass consumption during discharge could be attributed

to the corrosion reaction. This exact number is dependent on the discharge conditions such as the current and concentration. The modelled results of the corrosion shown in Figure 6.3 show that in the modelled system the corrosion consumes a similar fraction of the total consumed silicon, for the given circumstances. Because the corrosion reaction is modelled as a non-Faradaic reaction in COMSOL, charge transfer effects will have little to no effect on the corrosion rate in the model. Therefore, a higher discharge current will consume silicon at a higher rate in the discharge reaction, without increasing the consumption of silicon by the corrosion reaction. From literature [31] it is known that different discharge currents lead to different consumption rates of the silicon that cannot solely be explained by the increased consumption in the discharge mechanism. An improvement to the model would be a more detailed simulation of the corrosion mechanism for different discharge currents. Furthermore, the corrosion mechanism is in fact simplified to a single, non-Faradaic reaction that neglects the effect of charge distributions on the corrosion. As there is in fact a charge transfer in the half-reactions, an improvement to the presented model would be the introduction of these effects to the corrosion reaction.

In many experimental alkaline silicon-air batteries a current collector, or back contact is applied to the silicon anode. Even if no back contact is used on the silicon, the current is extracted from the battery and for this the silicon needs to be connected to an external circuit. This is typically done using a metal contact. As discussed in Section 2.7.2, a contact between a semiconductor and metal can lead to a Schottky barrier. If there is indeed a Schottky barrier, this can cause a drop in potential over the contact between the semiconductor and the metal. To limit the loss in this contact, it is important to be aware of the electron work function of the silicon used as anode in the battery. This can be found from the doping of the silicon. The material used as current collector or as contact should have an electron work function of similar magnitude as the used silicon. To validate that this claim holds, this needs to be investigated experimentally, as there is little published work pointing this out in the context of silicon-air batteries.

The height of the Schottky barrier will change, under a bias. In this model the height of the Schottky barrier is modelled as a constant voltage drop, independent of the exact discharge conditions of the battery. A closer representation of reality would be to implement the Schottky barrier in a more detailed way, where the contact actually dynamically behaves like a Schottky barrier, rather than as a static voltage drop.

The simulated discharge potentials for different discharge current densities were compared to experimental data. Certain similar trends were observed between the two. It was shown that for a higher discharge current density the discharge potential is somewhat lower compared to a lower discharge current density. This is to be expected, as ohmic losses will increase for higher current densities. This is in line with what was found in literature. In the simulated range of current densities there were three values that more or less lined up. However, the open circuit potential in the model was about 0.1 V higher than in the experimental data. The highest current density had a discharge potential that was about 0.1 V lower than the experimental data. Hence, in the model the spread of discharge potentials for different discharge current densities is too large. For the used parameter set the effect of the discharge current density on the discharge potential is more pronounced in the model than in experimental data. The model should be adapted slightly to better match this effect. A possibility is that the oxygen concentration or the effects if the oxygen in the air electrode in the model do not match the experimental situation. This concentration is influenced by the availability of oxygen in the air and the pore properties of the air electrode. In the work by Prins [37] it was shown that the amount of available oxygen in the air electrode quite significantly influences the discharge potential. The air electrode is not massively altered in comparison to the work by Prins [37].

The discharge potential in the model for different concentrations of the electrolyte was compared to experimental data. Especially for electrolyte concentrations between 2M and 5M the simulated results were quite similar to the experimental results. For lower concentrations (up to 1M), the experimental discharge potentials were notably lower. Effectively, the experimental results can be split in two groups: up to 1 M and 2 M and more. Durmus et al. [27] attribute this distinct separation to the surface reaction kinetics of the silicon electrode. The increased electrolyte concentrations lead to smaller over-potentials as a result from faster reaction kinetics. The lack of this separation in the simulated results may indicate

that the surface reaction kinetics in the simulations do not exactly resamble those in the work by Durmus et al. [27]. This might be to do with the fact that surface kinetics are generalised in the model to adapt it to the 1D model.

8

Conclusions

The initial goal of this work was to find a way to minimize the corrosion in an alkaline silicon air battery in an experimental setting. Due to the technical difficulties described in Chapter 4 the focus of this research was shifted to modelling of an alkaline silicon-air battery.

The goal of this research was to build a finite element model that was able to simulate the behaviour of an alkaline silicon-air battery, with inclusion of the parasitic corrosion reaction and the passivation mechanism. Both these mechanisms were implemented in the model.

The corrosion reaction was implemented as a non-Faradaic reaction. This is simplification of reality, since there is in fact a charge transfer in the corrosion mechanism in the half-reactions of the corrosion mechanism. However, the global effect of the corrosion mechanism that a significant portion of the silicon was consumed without contributing to the discharge mechanism was simulated for the given conditions.

The passivation mechanism was implemented in the model, and the passivating layer was shown to stop the discharge when the layer was big enough. An effect that might be underestimated in this model is the limited access to unconsumed silicon after the layer is formed. This can be attributed to the fact that the model is in 1D. This means that the layer is uniformly created on the surface of the electrode, rather than the heterogeneous growth one can expect, leaving certain parts passivated, and others still unpassivated.

The specific surface area of the silicon electrode was found to have a significant effect on the discharge performance of the silicon air battery. The value of the specific surface area of the silicon electrode was altered to ensure that the results resembled the experimental results the model was matched to. Increasing the specific surface area effectively increases the area of the silicon-electrolyte interface. This increase in discharge potential and discharge time is in line with literature [32, 38, 66].

A voltage drop was introduced, to resemble a metal-semiconductor contact in the battery model. For the given parameters this contact seems to make sure the OCP is close to what can be expected from literature.

The model was compared to experimental results by means of two parameters: the discharge current ans the electrolyte concentration . The effect of the discharge current on the discharge potential was as expected: higher discharge currents lead to lower discharge potentials. However, this effect was somewhat larger in the modeled results than what was observed in experimental work. The effect of the electrolyte concentration pm the discharge potential was also observed. Higher electrolyte concentrations yield higher discharge potential. This is to be expected from literature. However, from literature it is expected that an electrolyte concentration of up to 1 M would yield a distinctively lower discharge potential than for an electrolyte concentration of 2 M or more.

In conclusion, several improvements to the finite element model are proposed in this work. The passivation in a two step process rather than in a single deposition is proposed. A simplified corrosion mechanism is implemented in the model. A simplified Schottky barrier is implemented in the place of the metal-semiconductor interface. These three modifications to the model yield a closer representation of an actual silicon-air battery and this was verified with experimental data.

8.1. Outlook

Based on this work there are several recommendations to be made. They are listed below.

- As the experimental work was cut short, a first recommendation would be to investigate what these difficulties originate from. A careful suggestion was made in the experimental part of this work, that it might have to do with composition of the electrolyte. This can be a first step to investigate.
- The presented model is a 1D model. A more comprehensive model in 3D might be able to simulate the surface characteristics of the silicon-air battery better. In the presented model the passivation and corrosion mechanisms are simplified to fit in the 1D model. Especially in the case of the corrosion mechanism, this simplification to a non-Faradaic reaction was at the cost of loosing some of the effects in the corrosion mechanism concerning the half-reactions and their charge transfers.
- The presented model was tested for an n-type silicon anode. An interesting adaptation would be to investigate the effect that a p-type silicon would have in this model. Especially the Schottky barrier implemented in the model is likely to be influenced by this.
- The implemented Schottky barrier as illustrated in this work is a very crude voltage drop. Under a bias the barrier characteristics will change. This effect is neglected in this model. An interesting addition would be to implement a more detailed model for the metal-semiconductor contact.
- The influence of different metal contacts in the context of silicon-air batteries has not yet been explicitly researched. To get a more comprehensive understanding of this contact, experimental research can possibly provide helpful insights.
- From literature it is understood that a significant portion of the silicon is consumed in the parasitic corrosion mechanism. The author believes that for the further development of viable silicon-air batteries the corrosion should be mitigated and that further research should focus on the mitigation of the corrosion reaction.

Bibliography

[1] WHO, *Quantitative risk assessment of the effects of climate change on selected causes of death, 2030s and 2050s* (2014).

[2] *Paris agreement*, UN Treaty (Dec. 2015).

[3] D. P. Van Vuuren, P. A. Boot, J. Ros, A. F. Hof, and M. G. den Elzen, *The implications of the paris climate agreement for the dutch climate policy objectives* (PBL Netherlands Environmental Assessment Agency, 2017).

[4] CBS, *Hernieuwbare energie in nederland 2019*, Sept. 2020.

[5] D. Gielen, F. Boshell, D. Saygin, M. D. Bazilian, N. Wagner, and R. Gorini, "The role of renewable energy in the global energy transformation", Energy Strategy Reviews **24**, 38–50 (2019).

[6] P. Pinson, H. Madsen, et al., "Benefits and challenges of electrical demand response: a critical review", Renewable and Sustainable Energy Reviews **39**, 686–699 (2014).

[7] PBL, *Klimaat- en energieverkenning 2019* (2019).

[8] *Klimaat viewer*, Date accessed: November 22 2021, `https://www.knmi.nl/klimaat-viewer/grafieken-tabellen/meteorologische-stations/stations-maand/stations-maand_1991-2020`.

[9] F. Mulder, "Implications of diurnal and seasonal variations in renewable energy generation for large scale energy storage", Journal of Renewable and Sustainable Energy **6**, 033105 (2014).

[10] J. Torriti, "Understanding the timing of energy demand through time use data: time of the day dependence of social practices", Energy research & social science **25**, 37–47 (2017).

[11] C. B. Martinez-Anido, G. Brinkman, and B.-M. Hodge, "The impact of wind power on electricity prices", Renewable Energy **94**, 474–487 (2016).

[12] K. Schmidt-Rohr, "How batteries store and release energy: explaining basic electrochemistry", Journal of Chemical Education **95**, 1801–1810 (2018).

[13] K. Divya and J. Østergaard, "Battery energy storage technology for power systems—an overview", Electric power systems research **79**, 511–520 (2009).

[14] S. Rodrigues, F. Faria, A. R. Ivaki, N. Cafôfo, X. Chen, H. Mata-Lima, and F. Morgado-Dias, "Tesla powerwall: analysis of its use in portugal and united states", Int. J. Power Energy Syst **36** (2016).

[15] J. B. Broughton, P. U. Nyer, and C. E. Ybarra, "The economics of battery storage for residential solar customers in southern california", American Journal of Industrial and Business Management **11**, 924–932 (2021).

[16] G. E. Blomgren, "The development and future of lithium ion batteries", Journal of The Electrochemical Society **164**, A5019 (2016).

[17] CBS, *Jaarmonitor wegvoertuigen 2020*, June 2021.

[18] S. Hardman, A. Chandan, G. Tal, and T. Turrentine, "The effectiveness of financial purchase incentives for battery electric vehicles–a review of the evidence", Renewable and Sustainable Energy Reviews **80**, 1100–1111 (2017).

[19] J. H. L. Voncken, *The rare earth elements: an introduction* (Springer, 2016).

[20] M. Fleischer, *Recent estimates of the abundances of the elements in the earth's crust*, Vol. 285 (1953).

[21] T. Nazarewicz, "Cobalt: a critical commodity", Resource World, 52–53 (2016).

[22] K. J. Schulz, J. H. DeYoung, R. R. Seal, and D. C. Bradley, *Critical mineral resources of the united states: economic and environmental geology and prospects for future supply* (Geological Survey, 2018) Chap. F.

[23]S. Al Barazi, U. Näher, S. Vetter, P. Schütte, M. Liedtke, M. Baier, G. Franken, et al., “Cobalt from the dr congo–potential risks and significance for the global cobalt market”, Bundesanstalt für Geowissenschaften und Rohstoffe, Hannover (2017).

[24]G. André and M. Godin, “Child labour, agency and family dynamics: the case of mining in katanga (drc)”, Childhood **21**, 161–174 (2014).

[25]C. B. L. Nkulu, L. Casas, V. Haufroid, T. De Putter, N. D. Saenen, T. Kayembe-Kitenge, P. M. Obadia, D. K. W. Mukoma, J.-M. L. Ilunga, T. S. Nawrot, et al., “Sustainability of artisanal mining of cobalt in dr congo”, Nature sustainability **1**, 495–504 (2018).

[26]K. J. Schulz, J. H. DeYoung, R. R. Seal, and D. C. Bradley, *Critical mineral resources of the united states: economic and environmental geology and prospects for future supply* (Geological Survey, 2018) Chap. K.

[27]Y. E. Durmus, Ö. Aslanbas, S. Kayser, H. Tempel, F. Hausen, L. De Haart, J. Granwehr, Y. Ein-Eli, R.-A. Eichel, and H. Kungl, “Long run discharge, performance and efficiency of primary silicon–air cells with alkaline electrolyte”, Electrochimica Acta **225**, 215–224 (2017).

[28]H. Weinrich, Y. E. Durmus, H. Tempel, H. Kungl, and R.-A. Eichel, “Silicon and iron as resource-efficient anode materials for ambient-temperature metal-air batteries: a review”, Materials **12**, 2134 (2019).

[29]G. Cohn and Y. Ein-Eli, “Study and development of non-aqueous silicon-air battery”, Journal of Power Sources **195**, 4963–4970 (2010).

[30]G. Cohn, D. Starosvetsky, R. Hagiwara, D. D. Macdonald, and Y. Ein-Eli, “Silicon–air batteries”, Electrochemistry Communications **11**, 1916–1918 (2009).

[31]Y. E. Durmus, S. S. M. Guerrero, Ö. Aslanbas, H. Tempel, F. Hausen, L. De Haart, Y. Ein-Eli, R.-A. Eichel, and H. Kungl, “Investigation of the corrosion behavior of highly as-doped crystalline si in alkaline si–air batteries”, Electrochimica Acta **265**, 292–302 (2018).

[32]X. Zhong, H. Zhang, Y. Liu, J. Bai, L. Liao, Y. Huang, and X. Duan, “High-capacity silicon–air battery in alkaline solution”, ChemSusChem **5**, 177–180 (2012).

[33]Y. Li and J. Lu, “Metal–air batteries: will they be the future electrochemical energy storage device of choice?”, ACS Energy Letters **2**, 1370–1377 (2017).

[34]R. Bansal, P. Menon, and R. Sharma, “Silicon–air batteries: progress, applications and challenges”, SN Applied Sciences **2**, 1–17 (2020).

[35]A. Kraytsberg and Y. Ein-Eli, “Review on li–air batteries—opportunities, limitations and perspective”, Journal of Power Sources **196**, 886–893 (2011).

[36]*Air electrode*.

[37]J. Prins, “Alkaline pre-treatment of the air electrode in a silicon-air battery”, MA thesis (2020).

[38]D.-W. Park, S. Kim, J. D. Ocon, G. H. A. Abrenica, J. K. Lee, and J. Lee, “Controlled electrochemical etching of nanoporous si anodes and its discharge behavior in alkaline si–air batteries”, ACS applied materials & interfaces **7**, 3126–3132 (2015).

[39]P. Jakes, G. Cohn, Y. Ein-Eli, F. Scheiba, H. Ehrenberg, and R.-A. Eichel, “Limitation of discharge capacity and mechanisms of air-electrode deactivation in silicon–air batteries”, ChemSusChem **5**, 2278 (2012).

[40]E. Palik, O. Glembocki, and I. Heard Jr, “Study of bias-dependent etching of si in aqueous koh”, Journal of the Electrochemical Society **134**, 404 (1987).

[41]T. Kim, S. Park, and S. M. Oh, “Solid-state nmr and electrochemical dilatometry study on li+ uptake/extraction mechanism in sio electrode”, Journal of The Electrochemical Society **154**, A1112 (2007).

[42]M. M. Gauthier, *Engineered materials handbook*, Vol. 1 (ASM International, 1995).

[43]Y. E. Durmus, S. Jakobi, T. Beuse, O. Aslanbas, H. Tempel, F. Hausen, L. De Haart, Y. Ein-Eli, R.-A. Eichel, and H. Kungl, “Influence of dopant type and orientation of silicon anodes on performance, efficiency and corrosion of silicon–air cells with emim (hf) 2.3 f electrolyte”, Journal of The Electrochemical Society **164**, A2310 (2017).

[44]N. Raley, Y. Sugiyama, and T. Van Duzer, “(100) silicon etch-rate dependence on boron concentration in ethylenediamine-pyrocatechol-water solutions”, Journal of the Electrochemical Society **131**, 161 (1984).

[45]P. Allongue, H. Brune, and H. Gerischer, “In situ stm observations of the etching of n-si (111) in naoh solutions”, Surface science **275**, 414–423 (1992).

[46]P. Allongue, V. Costa-Kieling, and H. Gerischer, “Etching of silicon in naoh solutions: ii. electrochemical studies of n-si (111) and (100) and mechanism of the dissolution”, Journal of the Electrochemical Society **140**, 1018 (1993).

[47]H. Seidel, L. Csepregi, A. Heuberger, and H. Baumgärtel, “Anisotropic etching of crystalline silicon in alkaline solutions: i. orientation dependence and behavior of passivation layers”, Journal of the electrochemical society **137**, 3612 (1990).

[48]H. Seidel, L. Csepregi, A. Heuberger, and H. Baumgärtel, “Anisotropic etching of crystalline silicon in alkaline solutions: ii. influence of dopants”, Journal of the Electrochemical Society **137**, 3626 (1990).

[49]O. Glembocki, E. Palik, G. De Guel, and D. Kendall, “Hydration model for the molarity dependence of the etch rate of si in aqueous alkali hydroxides”, Journal of the Electrochemical Society **138**, 1055 (1991).

[50]E. Palik, V. Bermudez, and O. Glembocki, “Ellipsometric study of orientation-dependent etching of silicon in aqueous koh”, Journal of the Electrochemical Society **132**, 871 (1985).

[51]E. Palik, O. Glembocki, J. Rinko, and I. Heard Jr, “Current-voltage characteristics of heavily doped p-si in aqueous koh”, Journal of the Electrochemical Society **136**, 1420 (1989).

[52]I. Zubel, “Silicon anisotropic etching in alkaline solutions ii on the influence of anisotropy on the smoothness of etched surfaces”, Sensors and Actuators A: Physical **70**, 260–268 (1998).

[53]M. Pourbaix, “Atlas of electrochemical equilibria in aqueous solution”, NACE **307** (1974).

[54]P. A. Nikolaychuk, “The revised pourbaix diagram for silicon”, Silicon **6**, 109–116 (2014).

[55]A. Inoishi, T. Sakai, Y.-W. Ju, S. Ida, and T. Ishihara, “A rechargeable si–air solid state oxygen shuttle battery incorporating an oxide ion conductor”, Journal of Materials Chemistry A **1**, 15212–15215 (2013).

[56]D. A. Neamen, *Semiconductor physics and devices: basic principles* (New York, NY: McGraw-Hill, 2012).

[57]A. Smets, K. Jäger, O. Isabella, R. van Swaaij, and M. Zeman, *Solar energy: the physics and engineering of photovoltaic conversion, technologies and systems*, English (UIT Cambridge Limited, 2016).

[58]S. M. Sze, Y. Li, and K. K. Ng, *Physics of semiconductor devices* (John wiley & sons, 2006).

[59]N. Jacob, “Si-air battery: alkaline cell modelling in matlab (simscape)”, MA thesis (2020).

[60]*Comsol multiphysics reference manual* (Comsol, 2019).

[61]*1d isothermal lithium-air battery* (Comsol, 2021).

[62]*1d isothermal nickel-metal hydride battery* (Comsol, 2021).

[63]*1d isothermal zinc-silver oxide battery* (Comsol, 2021).

[64]E. J. Dickinson and A. J. Wain, “The butler-volmer equation in electrochemical theory: origins, value, and practical application”, Journal of Electroanalytical Chemistry **872**, 114145 (2020).

[65]H. B. Michaelson, “The work function of the elements and its periodicity”, Journal of applied physics **48**, 4729–4733 (1977).

[66]S. Sarwar, M. Kim, G. Baek, I. Oh, and H. Lee, “Transformation of silicon nanowire into nanopyramid in alkaline solution and its implication in silicon-air battery”, Bulletin of the Korean Chemical Society **37**, 997–1003 (2016).

[67]D. H. Everett, “Manual of symbols and terminology for physicochemical quantities and units, appendix ii: definitions, terminology and symbols in colloid and surface chemistry”, Pure and Applied Chemistry **31**, 577–638 (1972).

A

Appendix

Below are two images of the lasercutter used to etch lines in the silicon wafers.

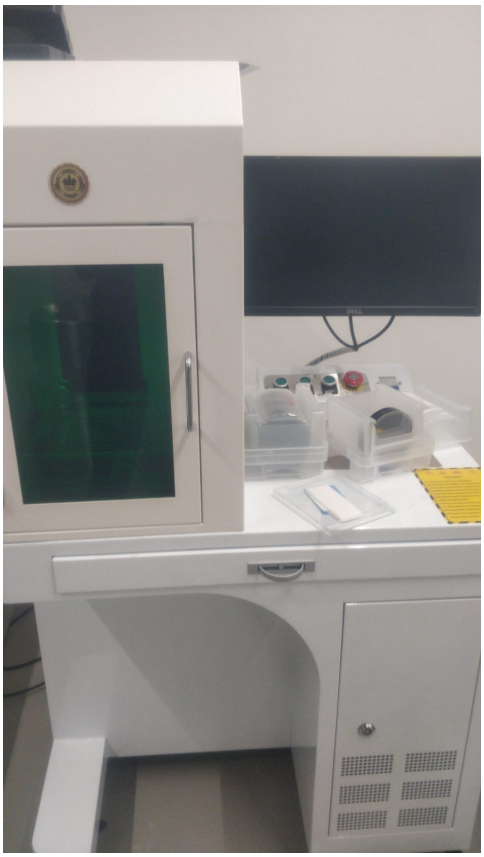

Figure A.1: An overview of the lasercutter setup

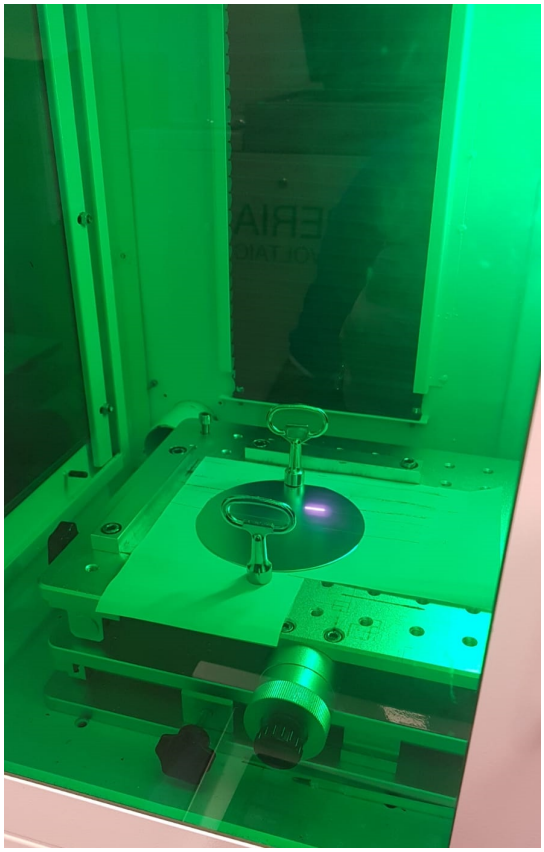

Figure A.2: The lasercutter in opperation

B

Appendix

In the table below the parameters used in the model are listed.

Table B.1: List of parameters

Parameter	Value	Unit	Description
L_{sep}	0.01	[m]	Length of separator
L_{pos}	7.5e-4	[m]	Length of positive electrode
L_{neg}	500e-6	[m]	Length of negative electrode
K_{pos}	10	[S/m]	Conductivity of positive electrode
K_{neg}	1e6	[S/m]	Conductivity of negative electrode
$\epsilon_{l0,pos}$	0.73	[-]	Initial porosity of positive electrode
$\epsilon_{s0,pos}$	1-$\epsilon_{l0,pos}$	[-]	Initial active material solid fraction of positive electrode
ϵ_{sep}	0.87	[-]	Porosity of separator
$\epsilon_{l0,neg}$	0.05	[-]	Initial porosity negative electrode
$\epsilon_{s0,neg}$	1-$\epsilon_{l0,neg}$	[-]	Initial active material solid fraction of negative electrode
$r_{pos,0}$	25e-9	[m]	Particle radius in the positive electrode
$r_{neg,0}$	1.5	[μm]	Particle radius in the negative electrode
$a_{pos,0}$	3*$\epsilon_{s0,pos}$/$r_{pos,0}$	[-]	Initial active specific surface area in positive electrode
$a_{neg,0}$	3*$\epsilon_{s0,neg}$/$r_{neg,0}$	[-]	Initial active specific surface area in negative electrode
$\alpha_{a,pos}$	0.013	[-]	Anodic transfer coefficient, positive electrode
$\alpha_{a,neg}$	0.025	[-]	Anodic transfer coefficient, negative electrode
$\alpha_{c,pos}$	0.074	[-]	Cathodic transfer coefficient, positive electrode
$\alpha_{c,neg}$	0.054	[-]	Cathodic transfer coefficient, negative electrode
R_{film}	50	Ωm^2	Film resistance across SiO2 film
Sol_{O_2}	0.4	[-]	Solubility factor of oxygen in electrolyte
$c_{O_2,ext}$	9.46	[mol/m^3]	External oxygen concentration in air at 1 atm
$c_{O_2,0}$	Sol_{O_2} * $c_{O_2,ext}$	[-]	Initial oxygen concentration in positive electrode
$c_{max,SiOH_4}$	0.09	[mol/m^3]	Solubility limit of $SiOH_4$ dissolved in electrolyte
c_{max,SiO_2}	0.0009	[mol/m^3]	Solubility limit of SiO_2 dissolved in electrolyte
$c_{SiO_2,init}$	1e-7	[mol/m^3]	Initial concentration of SiO2 in electrolyte
D_{Si+}	2.11e-9	[m^2/s]	Diffusion coefficient of Si+ in electrolyte
D_{O_2}	7e-10	[m^2/s]	Oxygen diffusion coefficient
D_{OH}	5.26e-9	[m^2/s]	Diffusion coefficient of OH-ion
D_K	1.96e-9	[m^2/s]	Diffusion coefficient of potassium ion
t_{plus}	0.22	[-]	Transport number
$d_{\ln f d \ln c_{sep}}$	-1.03	[-]	Activity dependence

k_a	1.11e-15	[$m^10/s/mol^3$]	Reaction rate coefficient anodic current
k_c	3.4e-17	[$m^7/s/mol^2$]	Reaction rate coefficient cathodic current
$k_{a,neg}$	1.11e-15	[m/s]	Reaction rate coefficient anodic current
$k_{c,neg}$	3.4e-17	[$m^10/s/mol^3$]	Reaction rate coefficient cathodic current
$i_{0,ref,Si}$	9.65e-1	[A/m^2]	Reference exchange current density Si metal
$i_{0,ref,pos}$	0.8	[A/m^2]	Reference exchange current density, negative electrode
$i_{0,ref,neg}$	0.1	[A/m^2]	Reference exchange current density, positive electrode
$E_{eq,neg}$	-1.69	[V]	Equilibrium potential negative electrode
$E_{eq,pos}$	0.4	[V]	Equilibrium potential positive electrode
n	4	[-]	Number of transferred electrons
T	298	[K]	Temperature
i_{app}	-0.05	[mA/cm^2]	Applied current density
a	1	[-]	Used in parametric sweep
A_{pos}	100	[cm^2/cm^3]	Specific surface area of positive electrode
A_{neg}	100	[cm^2/cm^3]	Specific surface area of negative electrode
$c_{l,init}$	5	[mol/dm^3]	Initial electrolyte concentration
$c_{oh,ref}$	0.4 * $c_{l,init}$	[mol/dm^3]	Reference electrolyte concentration
$c_{l,ref}$	5	[mol/dm^3]	Electrolyte salt reference concentration
$c_{0,ref}$	5	[mol/dm^3]	Solvent (water) reference concentration
ρ_{carbon}	2260	[kg/m^3]	Density of carbon
ρ_{SiOH_4}	1800	[kg/m^3]	Density of SiOH4
ρ	1500	[kg/m^3]	Electrolyte solution density
ρ_{Si}	2330	[kg/m^3]	Density of Si
ρ_{SiO_2}	2650	[kg/m^3]	Density of SiO2
ρ_{H_2O}	997	[kg/m^3]	Density of H2O
ρ_{O_2}	1141	[kg/m^3]	Density of O2
ρ_{OH}	1	[kg/m^3]	Density of OH
MW_{SiOH_4}	96.113	[kg/m^3]	Molecular weight of SiOH4
MW_{Si}	28.0855	[g/mol]	Molecular weight of Si
MW_{SiO_2}	60.08	[g/mol]	Molecular weight of SiO2
MW_{OH}	17.008	[g/mol]	Molecular weight of OH
MW_{H_2O}	18.015	[g/mol]	Molecular weight of H_2O
MW_{O_2}	15.999	[g/mol]	Molecular weight of O2
MW_K	39.1	[g/mol]	Molecular weight of K
σ_{film}	6.7e-4	[S/cm]	Film conductivity
σ_0	0	[S/m]	initial film thickness
SC_{PER,SiO_2}	0	[-]	Stoichiometric coefficient for porous electrode reaction
$SC_{PER,SiOH_4}$	-1	[-]	Stoichiometric coefficient for porous electrode reaction
$R\_d_{nf,SiOH_4}$	0	[$mol/m^3/s$]	Reaction rate non faradaic reaction SiOH4
R_d_{nf,SiO_2}	0.001	[$mol/m^3/s$]	Reaction rate non faradaic reaction SiO2
$R\_d_{cor,SiOH_4}$	0.005	[$mol/m^3/s$]	Reaction rate of SiOH4 in corrosion
$R\_i_{src,nf}$	0.001	[$mol/m^3/s$]	Overall reaction rate non faradaic
R_i_{src,cor_2}	0.001	[$mol/m^3/s$]	Overall reaction rate corrosion
$E_{eq,schottky}$	0.36	[V]	The barrier between the contact and the silicon wafer